
**FEDERAL UNIVERSITY OF CEARÁ**

**CENTER OF TECHNOLOGY**

**DEPARTMENT OF METALLURGICAL AND MATERIALS ENGINEERING**

**POSTGRADUATE PROGRAM IN MATERIALS SCIENCE AND ENGINEERING**

**MASTER DEGREE IN MATERIALS SCIENCE AND ENGINEERING**

**ARTHUR VILA NOVA ALBUQUERQUE LIMA**

# THERMAL SIMULATION OF TIG WELDING USING EBFVM AND DEEP LEARNING

**FORTALEZA**

**2023**

ARTHUR VILA NOVA ALBUQUERQUE LIMA

# THERMAL SIMULATION OF TIG WELDING USING EBFVM AND DEEP LEARNING

Dissertation submitted to the Postgraduate Program in Materials Science and Engineering of the Center of Technology of the Federal University of Ceará, as a partial requirement for obtaining the title of Master in Materials Science and Engineering. Concentration Area: Processes of Transformation and Degradation of Materials

Advisor: Prof. Dr. Francisco Marcondes

FORTALEZA

2023

Dados Internacionais de Catalogação na Publicação
Universidade Federal do Ceará
Sistema de Bibliotecas
Gerada automaticamente pelo módulo Catalog, mediante os dados fornecidos pelo(a) autor(a)

---

L696t Lima, Arthur Vila Nova Albuquerque.
Thermal simulation of TIG welding using EbFVM and Deep Learning / Arthur Vila Nova Albuquerque Lima. – 2023.
92 f. : il. color.

Dissertação (mestrado) – Universidade Federal do Ceará, Centro de Tecnologia, Programa de Pós-Graduação em Engenharia e Ciência de Materiais, Fortaleza, 2023.
Orientação: Prof. Dr. Francisco Marcondes.

1. TIG welding. 2. Austenitic stainless steel. 3. Numerical simulation. 4. EbFVM. 5. Deep learning. I. Título.

CDD 620.11

---

ARTHUR VILA NOVA ALBUQUERQUE LIMA

# THERMAL SIMULATION OF TIG WELDING USING EBFVM AND DEEP LEARNING

Dissertation submitted to the Postgraduate Program in Materials Science and Engineering of the Center of Technology of the Federal University of Ceará, as a partial requirement for obtaining the title of Master in Materials Science and Engineering. Concentration Area: Processes of Transformation and Degradation of Materials

Approved on:

EXAMINATION BOARD

---

Prof. Dr. Francisco Marcondes (Advisor)
Federal University of Ceará (UFC)

---

Prof. Dr. Marcelo Ferreira Motta
Federal University of Ceará (UFC)

---

Prof. Dr. Elineudo Pinho de Moura
Federal University of Ceará (UFC)

---

Prof. Dr. Diego Parente Paiva Mesquita
Getulio Vargas Foundation (FGV)

Dedicated to my family and friends whose love, support and inspiration during these years were fundamental to my professional and academic development.

## ACKNOWLEDGEMENTS

To my father, Josimar, and my mother, Lucielda, love, education, and support were given to me. I would also like to thank my brother, Alexandre, my sister, Josiany, my grandmother, Lucia, and the rest of my family who supported me in all times of difficulty.

I would like to express my gratitude to my advisor, Dr. Francisco Marcondes, for all the knowledge shared and for his patience with the challenges encountered in this journey. This research would not have been successful without his help and support. I am also grateful to José Renê, Ivens Lima, and Khennedy Bacule. They contributed their time and knowledge, which were fundamental to the development of this research.

I would like to thank all LDFC members who contributed to the development of the simulator used in this project.

I would like to thank the Federal University of Ceará, in particular the Professors of the Department of Engineering and Materials Science, for all the knowledge transmitted and for providing my personal and professional growth.

I would also like to thank my colleagues from the master's degree program, especially Felipe Wendrio, who became a great friend to me on this journey.

To the special persons: Acácia, Adolfo, Alexsandro, Amêna, Anderson, Cândido, Cintra, Daniela, Danilo, Diaulas, Emanuela, Igor, Fabricio, Felipe, Gabrielle, Jaína, Janaina, Jorge, Karlos, Katlyn, Laresca, Lia, Lucas, Mário, Nara, Paulo, Pedro, Ramon, Renata, Ribamar, Samuel, and Vitória. Thanks for the advice and guidance along the way.

To everyone who directly or indirectly took part in my academic and professional development, thank you.

This study was financed in part by the Coordenação de Aperfeiçoamento de Pessoal de Nível Superior - Brazil (CAPES) - Finance Code 001.

“Predicting the future isn’t magic, it’s artificial intelligence.”

(Dave Waters)

## ABSTRACT

Due to the rapid technological growth worldwide, manufacturing sectors are becoming increasingly demanding in terms of the effectiveness of their solutions. As a result, companies are leveraging innovations and advanced technologies to meet market demands. Among them, welding can be highlighted, as a process that is continuously studied and presents a series of problems to be solved for the design and manufacturing community. Fusion welding is one of the categories of these processes existing in the literature, in which the union of materials is performed through the fusion of elements. The level of energy involved in this process can cause damage to the resulting structure if it is not properly treated or controlled. Investigating the variables that influence the process and analyzing the generated temperature fields are useful measures to prevent these problems. Numerical simulation is a tool frequently used in scientific and technological research, seeking to reduce the costs of experimental development, presenting highly precise results comparable to experimental ones. In the same sense, the field of artificial intelligence, with deep learning algorithms, has been widely used with great efficiency in prediction and low computational costs. Therefore, this study aims to use the Element-based Finite Volume Method (EbFVM) to perform numerical simulations and evaluate the thermal behavior of the Tungsten Inert Gas (TIG) autogenous welding process in austenitic stainless steels. The study also uses deep learning networks to predict the thermal cycles generated during the process. In addition, a comparison will be made between the experimental results in the literature with the numerical simulations and predictions obtained through deep learning. Based on the comparisons made, it is concluded that the applied methodologies were highly efficient in understanding the welding process behavior. This strategy proves to be an excellent option for future studies in the area.



**Keywords:** tig welding; austenitic stainless steel; numerical simulation; ebfvm; deep learning;

## RESUMO

Devido ao rápido crescimento tecnológico em todo o mundo, os setores de fabricação estão se tornando cada vez mais exigentes em relação à eficácia de suas soluções. Como resultado, as empresas estão se alavancando em busca de inovações e tecnologias avançadas para atender às demandas do mercado. Dentre eles, pode-se destacar a soldagem, um processo que é continuamente estudado e apresenta uma série de problemas a serem resolvidos para comunidade de projeto e fabricação. Soldagem por fusão é uma das categorias desses processos existentes na literatura, na qual é realizado a união de materiais através da fusão dos elementos. O nível de energia envolvido nesse processo pode causar danos à estrutura resultante, caso não seja adequadamente tratado ou controlado. Investigar as variáveis que influenciam o processo e analisar os campos de temperatura gerados são medidas úteis para se prevenir quanto a esses problemas. A simulação numérica é uma ferramenta frequentemente utilizada em pesquisas científicas e tecnológicas, que busca reduzir os custos do desenvolvimento experimental, apresentando resultados altamente precisos comparáveis aos experimentais. No mesmo sentido, área de inteligencia artificial, com algoritmos de aprendizado profundo, vem sendo bastante utilizada com uma ótima eficiência de previsão e baixos custos computacionais. Sendo assim, este estudo tem como objetivo utilizar o Método de Volumes Finitos Baseado em Elementos (EbFVM) para realizar simulações numéricas e avaliar o comportamento térmico do processo de soldagem TIG autógeno em aços inoxidáveis austeníticos. O estudo também busca prever os ciclos térmicos gerados durante o processo, utilizando redes de aprendizado profundo. Além disso, será realizada uma comparação entre os resultados experimentais da literatura com as simulações numéricas e previsões obtidas por meio do aprendizado profundo. Com base nas comparações realizadas, conclui-se que as metodologias aplicadas foram altamente eficientes na compreensão do comportamento do processo de soldagem. Essa estratégia se mostra uma excelente opção para estudos futuros na área.



**Palavras-chave:** soldagem tig; aço inoxidável austenítico; simulação numérica; ebfvm; aprendizado profundo;

## LIST OF FIGURES

## LIST OF TABLES

## LIST OF ABBREVIATIONS AND ACRONYMS

| | |
|---|---|
| $MAPE_m$ | Average MAPE |
| 2D | Two Dimensions |
| 3D | Three Dimensions |
| AC | Alternating Current |
| AI | Artificial Intelligence |
| AISI | American Iron and Steel Institute |
| AM | Arithmetic Mean |
| Ar | Argon |
| BEM | Boundary Element Method |
| C | Carbon |
| CFD | Computational Fluid Dynamics |
| CNNs | Convolutional Neural Networks |
| CPU | Central Processing Unit |
| Cr | Chromium |
| CSM | Computational Solid Mechanics |
| Cu | Copper |
| CV | Coefficient of Variation |
| CVFEM | Control Volume-Based Finite Element Method |
| CWM | Computational Welding Mechanics |
| DC | Direct Current |
| DL | Deep Learning |
| DNNs | Deep Neural Networks |
| EbFVM | Element-based Finite Volume Method |
| FDM | Finite Difference Method |
| Fe | Iron |
| FEM | Finite Element Method |
| FVM | Finite Volume Method |
| GM | Geometric Mean |
| GMAW | Gas Metal Arc Welding |
| GTAW | Gas Tunsgsten Arc Welding |
| He | Helium |

| | |
|---|---|
| HF | High-Frequency |
| LDFC | Computational Fluid Dynamics Laboratory |
| MAG | Metal Active Gas |
| MAPE | Mean Absolute Percentage Error |
| MIG | Metal Inert Gas |
| MLP | Multilayer Perceptron |
| MMAW | Manual Metal Arc Welding |
| Mn | Manganese |
| MSE | Mean Squared Error |
| MSLE | Mean Squared Logarithmic Error |
| N | Nitrogen |
| Ni | Nickel |
| PH | Precipitation Hardened |
| PM | Weighted Mean |
| PReLU | Parametric ReLU |
| ReLU | Rectified Linear Unit |
| RMSprop | Root Mean Squared Propagation |
| SAW | Submerged Arc Welding |
| SGD | Stochastic Gradient Descent |
| SMAW | Shielded Metal Arc Welding |
| TIG | Tungsten Inert Gas |
| UFC | Federal University of Ceará |
| UNS | Unifield National Standard |

**CONTENTS**

# 1 INTRODUCTION

Welding processes are present in practically all metal-mechanical industries with growing demands for their application in the world. The search for continuous improvement and technological innovations in the sector promotes a large and frequent development in this area (XIA; JIN, 2018; FAVI *et al.*, 2019). There are different welding processes, and the selection of a specific process depends on the intended application (MESSLER, 2008).

Among the most common processes currently applied in industry, Tungsten Inert Gas (TIG) welding is the procedure that joins elements by fusion, using a tungsten electrode (non-consumable), protected by a constant gas flow. Because it is a process with excellent quality and precision, it has applications in aerospace, nuclear, food, pharmaceutical, metal-mechanical sectors, and others (SINGH *et al.*, 2017; FRENCH *et al.*, 2018; DRAMICANIN *et al.*, 2019; GAUTAM *et al.*, 2019).

Due to the characteristics of the TIG process, several materials can be welded, but it is widely used in stainless steel, a type of alloy that has high resistance to corrosion, weldability, formability, and extensive service life (PANDYA *et al.*, 2021). These steels can be divided according to their predominant microstructure, such as austenitic stainless steels (HOLMBERG, 2002). This way, several types of research are being developed related to TIG welding with these steels (KUTELU *et al.*, 2018; GARG *et al.*, 2019).

The material used in the process is one of the parameters that directly influence welding. Therefore, it is of great importance to evaluate all factors that can cause problems in the resulting part. (SHAO *et al.*, 2019; ASADI *et al.*, 2020). One of the ways to prevent welding problems is using the simulation tool that approximates the thermomechanical behavior of the process. With good modeling of the welding process, approaching the boundary conditions of a real process, it is possible to analyze the behavior of the process through simulations. This does not mean that simulation will replace experimental studies since many parameters (input to simulations) come from experimental results (GOLDAK; AKHLAGHI, 2005).

In this context, models are developed seeking to better approximate the behavior of the heat source and how the heat transfer in the process is carried out. The double ellipsoidal model is well accepted and complete for electric arc welding processes and can be applied to the TIG process (VARGHESE *et al.*, 2012; PAVAN *et al.*, 2019).

Due to the complexity of existing problems in this area, the use of numerical methods is necessary. An approach that is still underutilized in the field of Computational Solid Mechanics

(CSM), but is precise and stable, is the Element-based Finite Volume Method (EbFVM) with unstructured meshes (PIMENTA; MARCONDES, 2019). This method can also be called the Control Volume-Based Finite Element Method (CVFEM). However, according to (MALISKA, 2004), this terminology is inappropriate because the method is based on finite volumes rather than finite elements. It only includes the definition of elements and their shape functions.

In this same context, other ways can be used to predict these behaviors. It can be highlighted the use of Artificial Intelligence (AI) for these applications, using machine learning algorithms to better understand the behavior of the welding process and generate results close to the real ones. In the last decades, efforts have been made in the search to develop this field in increasingly specific areas. The concept of deep learning, together with neural network architectures, can be inserted in this sense by using more layers and parameters, deepening the variables involved (SHINDE; SHAH, 2019)(MAHADEVAN *et al.*, 2021).

Several researchers have been working with this tool and are finding excellent results in various applications in the field of welding. Among them, Martínez *et al.* (2021) analyzed the Gas Metal Arc Welding (GMAW) process with machine learning and deep learning techniques, predicting the weld bead geometry. Jiao *et al.* (2021) has already worked with the Gas Tungsten Arc Welding (GTAW) process predicting weld penetration from end to end. Kesse *et al.* (2020) proposed an algorithm that can help human welders in the selection of final parameters to obtain a good weld quality in the TIG process as well. Sarkar *et al.* (2021) sought to predict and analyze the temperature field in submerged arc welding. In addition, this tool can also be used to monitor the actual welding process, as shown in a short review by Cai *et al.* (2019). Therefore, the study has the following objectives.

## 1.1 Objectives

### *1.1.1 General objectives*

The objective of this study is to analyze the thermal behavior of the autogenous TIG welding process applied to rectangular plates of austenitic stainless steels (316L, 316, and 304). The study will involve comparing the temperature distribution of experimental cases from the literature with numerical simulations using EbFVM, as well as with predictions generated by deep learning models. By conducting these comparisons, the study aims to gain a deeper understanding of the welding process and its associated thermal behavior.

### *1.1.2 Specific objectives*

- Model the autogenous TIG welding process applied to austenitic stainless steels;
- Validate the welding processes in experimental cases from literature with numerical simulations using EbFVM;
- Compare the simulated thermal cycles with the experimental ones, qualitatively (visual analysis) and quantitatively (Mean Absolute Percentage Error (MAPE) and Coefficient of Variation (CV) performance indices);
- Investigate the influence of spatial and temporal refinement on the thermal behavior of process;
- Predict thermal cycles for different welding configurations through numerical simulation;
- Analyze the computational cost of simulations performed;
- Investigate the main variables that influence the autogenous TIG welding process;
- Create a database with the main variables and the thermal cycles generated in numerical simulations for each set of corresponding parameters;
- Investigate the best hyperparameters to be applied in training the deep learning network;
- Build, train and test deep learning networks with data obtained from simulations;
- Compare the predictions of thermal cycles obtained with deep learning with the results found by numerical and experimental simulation, qualitatively and quantitatively.

## 1.2 Dissertation organization

This dissertation was divided into four main topics, seeking to complete the proposed objectives and fulfill all requirements as a partial requirement for obtaining the title of Master in Materials Science and Engineering.

The first topic (Chapter 2) makes a literature review presenting the main concepts that were necessary for the development of research. Themes about stainless steels, welding processes, computational welding mechanics, thermal processes in welding, numerical methods and machine learning were addressed.

For the second topic (Chapter 3) numerical simulations were performed using EBFVM to analyze the thermal behavior in TIG welding process with austenitic stainless steels. For the next topic (Chapter 4) deep learning networks were constructed, trained and tested to predict the thermal cycle of same process of previous chapter with TIG welding in austenitic

stainless steels, but with lower computational costs.

Finally, the fourth topic (Chapter 5) summarizes the conclusions obtained in previous chapters.

# 2 LITERATURE REVIEW

In the field of welding and computational mechanics, various areas of focus contribute to a comprehensive understanding of the subject matter. This chapter presents an overview of several key subsections. Firstly, there is a discussion on stainless steel, with a specific focus on austenitic stainless steel. The chapter then moves on to explore welding processes, including the widely used Tungsten Inert Gas (TIG) welding method. Computational welding mechanics is the next topic, where numerical methods are used to model and analyze welding processes. The thermal processes that occur during weldings, such as heat transfer and the welding thermal cycle, are also covered. Additionally, the chapter highlights the element-based Finite Volume Method as an essential numerical method in welding. Lastly, the chapter touches upon the main concepts and tools used in machine learning, particularly Deep Learning (DL). Through the exploration of these subsections, readers can gain a comprehensive understanding of welding, computational mechanics, and machine learning.

## 2.1 Stainless steels

Stainless steels are formed by high alloy steels that contain Fe and Cr as the main metallic elements in alloy composition. Chromium is largely responsible for the good corrosion resistance of these materials, both at ambient and high temperatures, so must have at least 10.5%wt Cr for steel to belong to the stainless steel group (LIPPOLD; KOTECKI, 2005). In addition to this property, these steels have higher ductility, strength and hardness (STEELS, 2021).

New compositions can be developed in search of specific properties with the addition of several other alloying elements, such as nickel, manganese, silicon, titanium, and molybdenum, among others (ANGELO; BAVISANKAR, 2019).

Experiments involving chromium-added steels were initially developed by the Frenchman Berthier in 1821. After that, other studies were initiated by Germans and British around 1910. However, with the increasing interest in corrosion-resistant steels for industrial applications, an effort extra development was done to start the commercialization of these alloys. Finally, in 1920, in the United States, commercial production of stainless steel began. (LIPPOLD; KOTECKI, 2005; ANGELO; BAVISANKAR, 2019). These alloys are available through coils, sheets, bars, and wires and can be applied in food, aerospace, automotive, and medical industries,

among others (YOUSSEF, 2016).

Stainless steels are classified by their predominant metallurgical phase, subdividing into five groups, three basic groups (ferritic, austenitic, and martensitic) and two derived groups (duplex and precipitation hardened) (YOUSSEF, 2016). Duplex steels have approximately 50% of austenite phase and 50% of ferrite phase, mixing the properties of interest of each phase. Precipitation Hardened (PH) is hardenable by aging heat treatment and form strengthening precipitates (LIPPOLD; KOTECKI, 2005). Figure 1 illustrates this division. In addition, a comparison of some properties of each type of stainless steel is shown in Table 1.

Figure 1 – Basic and derived groups of stainless steel alloys.

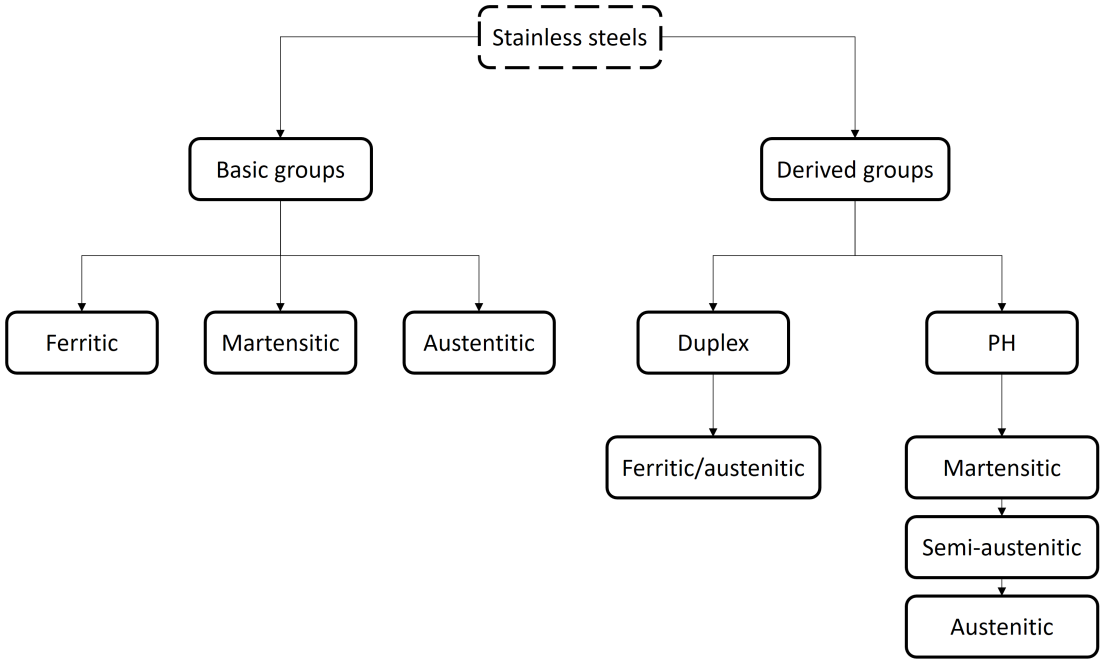


Source: Adapted from Youssef (2016).

Table 1 – Comparative properties of stainless steels.

| Alloy group | Austenitic | Ferritic | Martensitic | Duplex | Precipitation hardening |
|---|---|---|---|---|---|
| Magnetic response | Generally, no | Yes | Yes | Yes | Yes |
| Work hardening | Very high | Medium | Medium | Medium | Medium |
| Corrosion resistance | High | Medium | Medium | Very high | Medium |
| Hardenable | By cold work | No | Quench & temper | No | Age hardening |
| Ductility | Very high | Medium | Low | Medium | Medium |
| High temperature resistance | Very high | High | Low | Low | Low |
| Low temperature resistance | Very high | Low | Low | Medium | Low |
| Weldability | Very high | Low to high | Low | High | High |

Source: Adapted from Steels (2021).

The American Iron and Steel Institute (AISI) uses a three-digit series number, followed by a letter to indicate an additional characteristic, to represent stainless steel. Series 400 (405-409-429-430-434-436-439-442-444-446) for ferritic, series 400 (403-410-414-416-420-422-431-440) for martensitic, and series 200 Iron (Fe)-Chromium (Cr)-Manganese (Mn) and 300 series Fe-Cr-Nickel (Ni) for austenitic. The Unifield National Standard (UNS) also represents stainless steels using a five-digit code (YOUSSEF, 2016).

### *2.1.1 Austenitic stainless steels*

Austenitic stainless steels are widely used due to their versatile properties, making them suitable for a range of applications, including kitchenware, connections, welded constructions, lightweight transportation equipment, parts of ovens and heat exchangers, and materials for chemical environments. These steels were first invented in Germany and are now produced on a global scale, with this country being the world's leading producer (PLAUT *et al.*, 2007; YOUSSEF, 2016).

These steels generally have good ductility, toughness, excellent resistance to atmospheric or high-temperature corrosion, and good weldability. In addition, their cost is higher when compared to martensitic and low to medium Cr content ferritic (LIPPOLD; KOTECKI, 2005).

The addition of some alloy elements can stimulate the formation of austenite, such as Ni, Carbon (C), Nitrogen (N) and Copper (Cu). Nickel is added at values above 8wt%, while carbon and nitrogen also improve the strength of steel. Some suffixes can be inserted in

the designation given by AISI to illustrate changes in the original configuration of alloy type. Reinforcement through nitrogen is illustrated with the suffix "N". The "L" suffix represents lower carbon levels around 0.03wt% and the "H" around 0.1wt% (LIPPOLD; KOTECKI, 2005).

Austenitic stainless steels include alloys of 200 and 300 series according to AISI, with the second series being the most used within this steel class. For the 200 series alloys, there are high levels of carbon, manganese, and nitrogen, having less nickel content when compared to the 300 series alloys. Among the most used are types 304 (the most used), 316, 321, 347, and their variants (LIPPOLD; KOTECKI, 2005; YOUSSEF, 2016). Figure 2 illustrates the family of austenitic stainless steels.

Figure 2 – Austenitic stainless steels family.

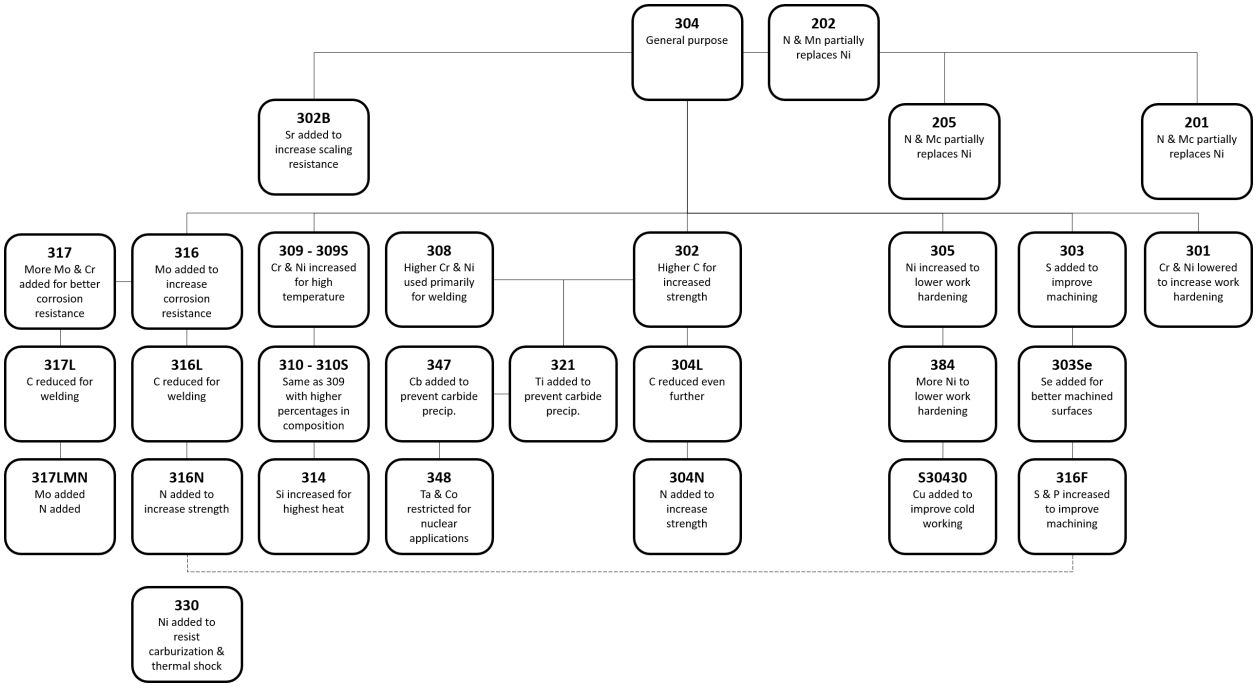


Source: Adapted from McGuire (2008).

## 2.2 Welding processes

Welding is the oldest manufacturing art form used for joining materials. In 1881, the use of the electric arc to melt metals was pioneered in France, marking a significant step towards modern welding. The technique was later employed in Russia for welding metals with consumable metal electrodes. The first patents for metal arc welding were granted in the United States in 1889. During this time, a process using mixtures of air and organic fuels was also developed. (MESSLER, 2008).

The welding process is generally more advantageous, with many options of process

modalities, applications to various materials, manual or automatic operation, can be portable internally or externally, and has an acceptable average cost. However, it has some disadvantages such as the fact that it is difficult to disassemble joints welding without destroying the parts that have details. Process heat can affect base properties and cause distortion or residual stresses. Furthermore, good operator skills and a high equipment cost may be necessary depending on the specific application (MESSLER, 2008).

Typically, the processes are classified into two different groups, welding with pressure and fusion welding, one using pressure to join the materials and the other using base metal fusion to make the weld. Among the pressure welding processes, there are the types of resistance, cold, friction, diffusion, explosive, and magnetically impelled arc butt. For fusion, there is Manual Metal Arc Welding (MMAW), Submerged Arc Welding (SAW), Gas Tunsgsten Arc Welding (GTAW) or Tungsten Inert Gas (TIG), Gas Metal Arc Welding (GMAW), laser, and the electron beam (NORRISH, 2006). Figure 3 illustrates some important welding processes.

Figure 3 – Some important welding processes.

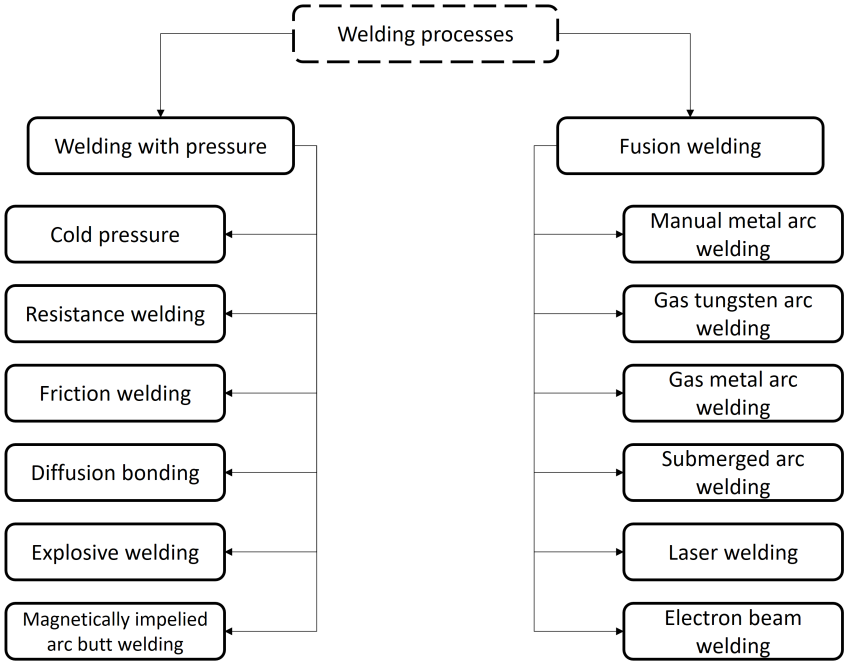


Source: Adapted from Norrish (2006).

Shielded Metal Arc Welding (SMAW) or MMAW is a widely used process because it has simpler equipment, can be portable, and offers a wide variety of consumables. However, it has low operational efficiency and requires considerable operator skill. The process applies an arc as a source of heat, which is protected by gases generated in the electrode coating itself and

by the slag formed (NORRISH, 2006).

Submerged Arc Welding (SAW) is a process that has high deposition rates, automatic operation, and offers many flux/wire combinations. Because the arc is protected by a molten slag, there is no visible arc radiation. However, it is a procedure that can only be used in flat or horizontal positions and is normally used for parts with a thickness above 6 mm (NORRISH, 2006).

Gas Metal Arc Welding (GMAW) can also be called Metal Inert Gas (MIG) or Metal Active Gas (MAG). It is a process that allows continuous operation because the consumable wire is fed continuously, resulting in a high deposition rate, but with a lower heat input compared to SMAW and SAW. Additionally, the arc is formed between the tip of a consumable wire and the workpiece, being protected by an inert gas, resulting in lighter slag and low hydrogen, which reduces post-weld cleaning and the risk of cold cracking (NORRISH, 2006).

Laser welding has a low-power confined heat source that can be used as an alternative to fusion welding. The process provides deep penetration at high power, and reduces distortion and thermal damage, but it has a high equipment cost (NORRISH, 2006).

Electron beam welding is a process that also has a confined source but with very high energy density, as a beam of electrons is accelerated to a high voltage. Vacuum is normally required, and it has a high depth-to-width ratio of welds and a high cost as well (NORRISH, 2006).

### *2.2.1 TIG welding*

TIG welding is an electric arc welding process created between a non-consumable tungsten electrode and the material to be welded. Weld protection against atmospheric gases is done by an inert gas, such as Argon (Ar) or Helium (He), which does not react with the molten metal (TIMINGS, 2008). Figure 4 shows the TIG welding process in detail.

Figure 4 – The TIG process.

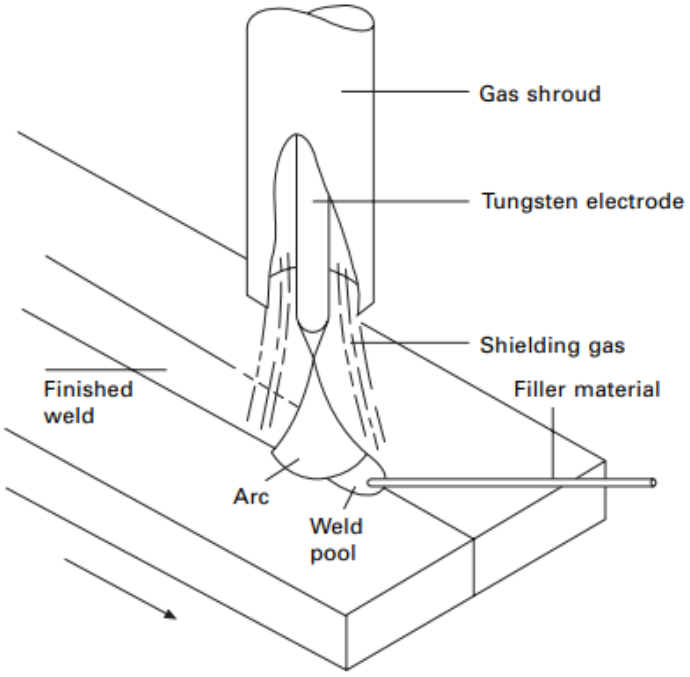


Source: Norrish (2006).

The process has a stable arc and excellent control of welding results, having applications in all welded materials, in particular stainless steel, light metals with aluminum and magnesium alloys, and copper, with the exception of lead and zinc (WEMAN, 2012). Furthermore, the arc density is relatively high, with low deposition rates resulting in good joint quality. (NORRISH, 2006).

Among the parameters of TIG welding, the welding current is the one that most influence the process, having a direct influence on the shape of the bead, speed, and quality of the weld. Most of these processes use direct current to the negative electrode resulting in greater penetration into the weld and higher travel speed. Welding voltage is related to the shape of the fusion zone and the weld reinforcement and can be fixed or flexible depending on the application and equipment. On the other hand, the welding speed does not influence the formation of the weld pool, only the volume of molten material (KUTELU *et al.*, 2018).

Shielding gases can influence the result of the welding process. Argon gas is the most used in TIG welding, in addition to being cheaper than helium gas, which is also applied. This gas has a low ionization potential that facilitates the ignition of an electric arc and shields the molten pool. Normally, argon is used with carbon and stainless steel and thin aluminum alloy components. On the other hand, helium is applied to thicker aluminum parts and materials with high conductivity (KUTELU *et al.*, 2018). Figure 5 shows a comparison of gases argon and

helium.

Figure 5 – Comparison between Ar and He gases.

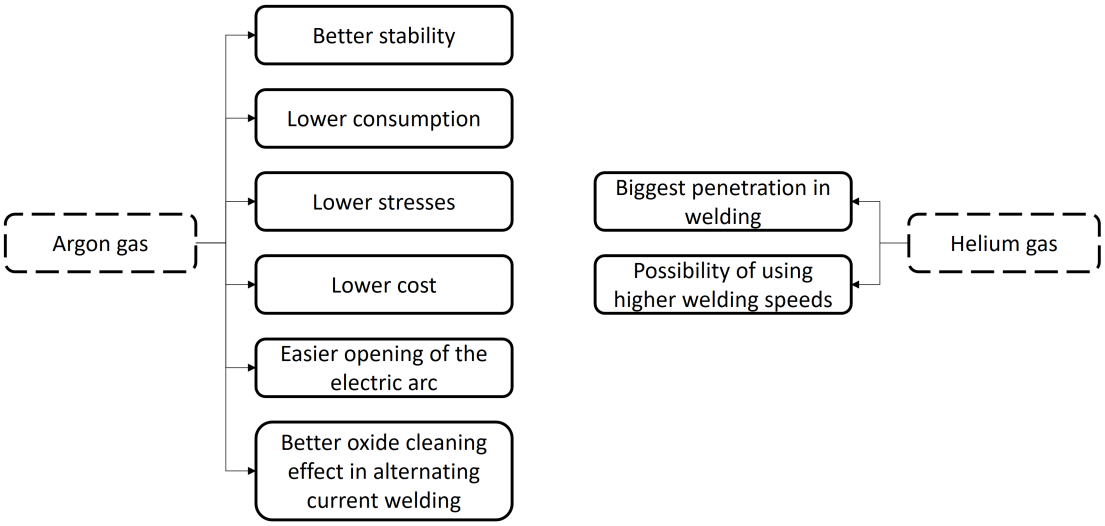


Source: Adapted from Marques *et al.* (2011)

The basic equipment used in the process includes the welding torch (with the electrode included), a High-Frequency (HF) generator, a power source, a gas tube with a regulator, and control equipment. The torch can be both air-cooled and water-cooled and can handle a maximum current limit of 200 A and 400 A, respectively. Additionally, they must be easy to handle and well-insulated. The tungsten electrode must have good electron emission and thermal conductivity with low electrical resistance but with a high melting point to prevent consumption during the process. The HF generator generates a spark that indicates the initial conduction path for the low-voltage welding current. The energy source can be Direct Current (DC) or Alternating Current (AC), depending on the material used in the process. The control equipment can be used for pre-flow and post-flow of shielding gas and for controlling the HF generator. Its importance increases with the level of automation in the procedure (WEMAN, 2012). Figure 6 illustrates a schematic diagram of TIG welding equipment.

Figure 6 – Schematic diagram of TIG welding equipment.

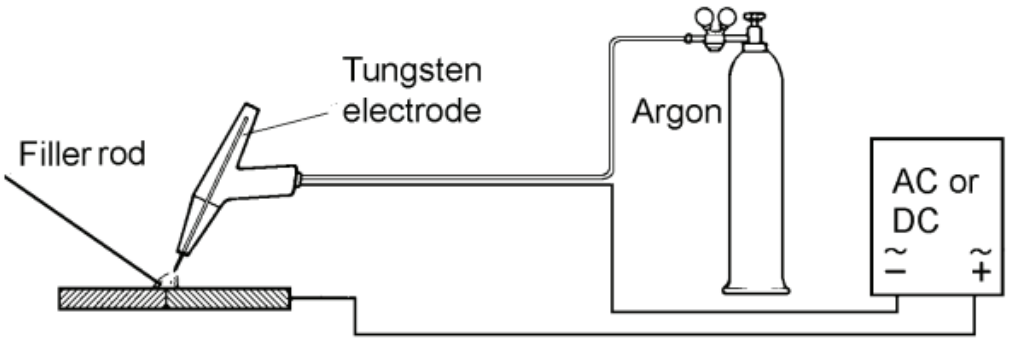


Source: Weman (2012).

Furthermore, in the TIG process, the filler metal is applied directly to the weld pool by being melted and joined with the workpiece material in the region. However, this welding can also be done without this metal by melting the heated edges of the part. This option is called autogenous welding (KUTELU *et al.*, 2018).

## 2.3 Computational welding mechanics

Computational Welding Mechanics (CWM) uses methods and models to deal with the welding process, including the modeling of heat generation, melting pool phenomena, thermal stresses, and large plastic deformations. Welding is a multiphysics problem involving fluid flow, heat transfer and conduction, and deformation. Therefore, the equations that represent the physics of these phenomena must be coupled to obtain a solution. However, there are simplified models that can be used to facilitate the process. One of them replaces the physics in the weld with a heat input model, which has a weaker coupling. The division of the problem into thermal and mechanical phases (staggered approach) together with the choice of a fixed coordinate system are common approaches (LINDGREN, 2007). In most CWM studies, the heat input distribution is prescribed and calibrated with experimental measurements, while the fluid flow is ignored. Therefore, if the fluid flow is not the main objective of the study, the CWM scheme can be represented as shown in Figure 7.

Figure 7 – Classical CWM modelling scheme of fusion welding without a welding process model and without fluid flow.

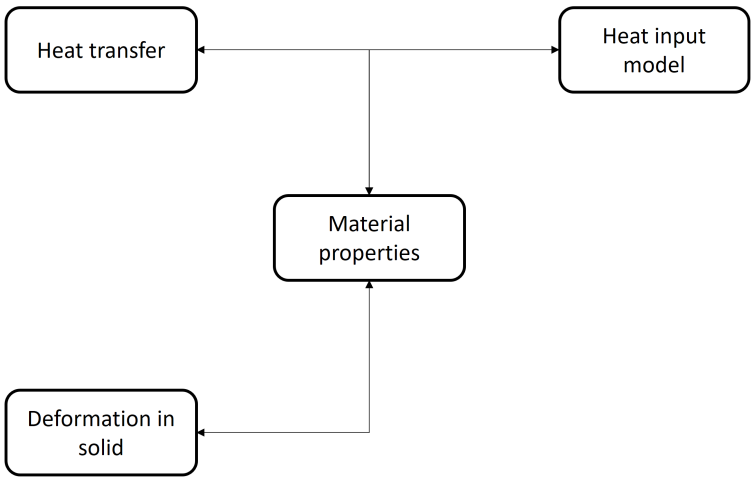


Source: Adapted from Lindgren (2007).

The approach used in CWM models does not take into account the physical characteristics of the weld pool. Instead, the focus is on the fundamental principle of energy conservation, which is used to analyze the thermal behavior of the problem. In CWM, nonlinear heat conduction solutions are used to analyze the heat transfer, which is more direct and requires smaller models when compared to nonlinear deformation solutions. Although the physics of the weld pool is not explicitly considered in the approach, the thermal analysis is still effective in predicting the behavior of the system. By analyzing the heat transfer, the model can provide valuable insights into the temperature distribution and thermal history of the weld, which are crucial for determining the quality of the weld. Additionally, the use of nonlinear heat conduction solutions makes it possible to model complex thermal behaviors with relative ease, providing a powerful tool for the analysis of welding problems (GOLDAK; AKHLAGHI, 2005; LINDGREN, 2007).

While in conduction a scalar temperature field is used, in deformations a tensor field is used. By specifying the heat input, the temperature field in the neighborhood of the melt pool can be found. Heat source models prescribe temperature or flux at the domain boundary near the pool or describe the source term. The solution to the problem can be unique, however, it depends on the existence of phase changes and their thermal properties (GOLDAK; AKHLAGHI, 2005; LINDGREN, 2007).

The great foundation of welding sources comes from experimental observations or detailed models of the welding process. Since the physics of this phenomenon is complex, thermal models of heat sources are developed to simplify the mathematics of the process. The classification of models can be given in categories from the first to the fifth generation, this order of complexity (GOLDAK; AKHLAGHI, 2005):

- **First generation** – Three different heat source models were used: point, linear, and flat.
- **Second generation** – Distributed area and volume sources based on heat conduction were used;
- **Third generation** – Tried to predict the liquid-solid interface based on energy equations;
- **Fourth generation** – Fluid dynamics equations were used in molten weld pool;
- **Fifth generation** – Complemented the previous models with the magnetohydrodynamics equations of welding.

Kinematic models illustrate the direction of heat flows (in plane, cross-section, radial, or freely in three dimensions). In reality, in a 3D simulation, the computational cost is the highest. However, it is possible to restrict a dimension of analysis, in order to obtain lower costs, keeping a good precision of results. (GOLDAK; AKHLAGHI, 2005).

Welding deformation is one of the main problems that are investigated in the process. In plate welding, the main cause of deformation is the shrinkage of the weld in longitudinal and transverse directions, which generates transverse or longitudinal contraction effects, bending, distorting in angular shape, or warping. The influence of welding speed related to the heat diffusivity has great weight in the analysis of process behavior (LINDGREN, 2007).

The basic concepts of heat transfer and numerical methods are necessary for the formulation and discretization of thermal simulation of the welding process.

## 2.4 Thermal processes in welding

### *2.4.1 Heat transfer*

For thermal analysis of the welding process, the fundamental principle is energy conservation. Thus, the development of heat transfer theory is focused only on energy, ignoring stress, strain, and displacement. Generally, in a thermal problem, the material properties, and initial and boundary conditions are used as parameters. The mathematics of heat transfer in welding is expressed as a nonlinear partial differential equation having the temperature,

$T(x,y,z,t)$, as a function of spatial and time coordinates, occurring at all points in the domain, $\Omega$ (GOLDAK; AKHLAGHI, 2005):

$$\frac{Dh}{Dt} + \nabla.(-k\nabla T) + Q = 0, \tag{2.1}$$

with:

$Q$ - source or sink rate of heat in $\Omega$ $(W/m^3)$,

$k$ - thermal conductivity $(W/mK)$,

$h$ - specific enthalpy $(J/Kg)$.

The increment in specific enthalpy, if no phase change occurs, can be expressed as:

$$dh = cdT, \tag{2.2}$$

with:

$c$ - volumetric specific heat $(J/m^3K)$.

For Equation 2.1, the first term represents the rate of change of specific enthalpy, the second term is the flow of heat into or out of surroundings, and the last term is the source of heat generation.

Boundary conditions for prescribed temperature (essential) or prescribed heat flux (natural) must be satisfied within the domain boundary $\Omega$. The essential condition can be defined as:

$$T(x,y,z,t) = T_1(x,y,z,t), \tag{2.3}$$

on the boudary $S_1$ com $(x,y,z) \in S_1 : t > 0$.

The natural condition can be defined as:

$$k_n \frac{\partial T}{\partial n} + q + h_c(T - T_0) + \sigma\varepsilon(T^4 - T_0^4) = 0 \tag{2.4}$$

on the boudary $S_2$ com $(x,y,z) \in S_2 : t > 0$,

with:

$k_n$ - thermal conductivity normal to the surface $(W/mK)$,

$q$ - a prescribed flux $(W/m^2)$,

$h_c$ - heat transfer coefficient for convection $(W/m^2K)$,

$\sigma$ - Stefan-Boltzmann constant $(W/m^2K^4)$,

$\varepsilon$ - emissivity,

$T_0$ - the ambient temperature for convection and/or radiation $(K)$.

Finally, the initial condition can be specified in terms of $(x,y,z) \in \Omega$:

$$T(x,y,z,0) = T_0(x,y,z), \tag{2.5}$$

### *2.4.2 Welding thermal cycle*

In most welding processes, especially in melting processes, heating in the welded joint can generate temperatures ranging from room temperature to values above the liquidus temperature of the material. The temporal history of temperatures at a given point illustrates the welding thermal cycle. The dimensions of welded joints, thermophysical properties of the material, initial and boundary conditions, parameters of the heat source, and the position of the material in relation to the source are characteristics that influence the thermal cycles. The analysis of this history is important because it indicates the effects caused by the structure-property relationship of the process. Figure 8 shows the behavior of these cycles (KARKHIN, 2019; MESSLER, 2008).

Figure 8 – Temperature and heating/cooling rate as functions of time for a point.

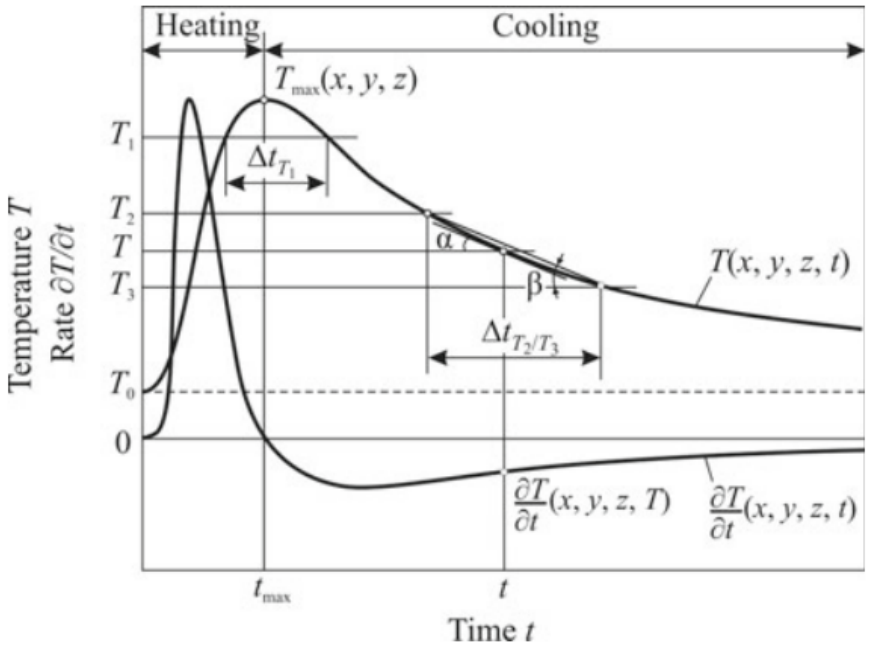


Source: Karkhin (2019).

The thermal cycle $T(x,y,z,t)$ at an arbitrary point $(x,y,z)$ represented in Figure 8 exemplifies a single-step welding process with a simple power distribution in time and space. The second curve $\frac{\partial T}{\partial t}(x,y,z,t)$ shows the rate of temperature versus time at which it can be used to better understand the behavior of a process. In addition, other thermal cycle information

may be relevant in an analysis, such as the maximum temperature of the cycle or also called peak temperature $T_{max}(x,y,z)$, residence time of metal $\Delta t_{T_1}$ which indicates the time the curve was above the temperature $T_1$, or the mean rate of heating and cooling $\left(\frac{\partial T}{\partial t}\right)_m = \left(\frac{T_3 - T_2}{\Delta t_{T_2/T_3}}\right)$ (KARKHIN, 2019).

Furthermore, Experimentally, this cycle can be acquired through thermocouples at the position in which we want to collect and understand the historical temporal behavior of temperature (MESSLER, 2008).

## 2.5 Numerical methods

In general, finding exact solutions to engineering problems is not easy. Approximate solutions can be developed using numerical methods, such as the Finite Difference Method (FDM), Finite Element Method (FEM), Finite Volume Method (FVM), Boundary Element Method (BEM), Element-based Finite Volume Method (EbFVM), among others (MALISKA, 2004; CORDAZZO, 2006).

The finite difference method is one of the oldest and simplest methods that solve differential equations, approximating the solution using different difference schemes. There are three ways to express derivatives with this method, forward, backward, and central scheme (CHAKRAVERTY *et al.*, 2019).

The finite element method has a methodology of numerically discretizing with finite elements so that the entire domain is partitioned using any shape in general. In addition to that converts differential equations into algebraic equations. This method is widely applied in fields of science and engineering (CHAKRAVERTY *et al.*, 2019). Figure 9 illustrates a comparison of discretization between the FDM and FEM.

Figure 9 – (a) Finite difference and (b) finite element discretization of arbitrary object.

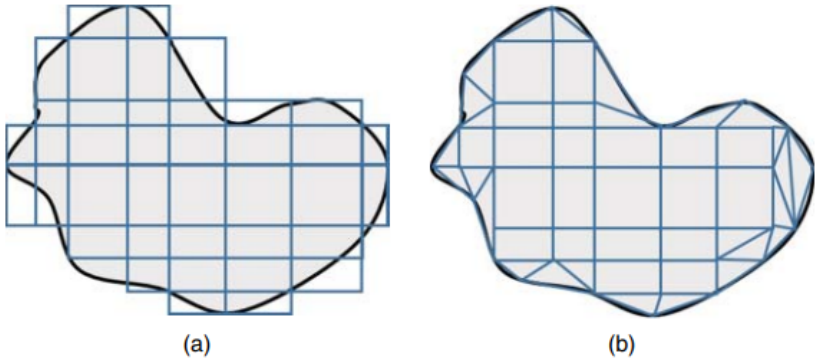


Source: Chakraverty *et al.* (2019).

The finite volume method uses an approach in which volumes are investigated in discrete places over a meshed geometry. This method has a conservation property that makes it more preferred compared to others, mainly for applications of fluid flow and heat and mass transfer simulations. In addition, it can be formulated in non-regulated polygonal meshes and with easy implementation for boundary conditions (CHAKRAVERTY *et al.*, 2019). Figure 10 illustrates the representation of a structured mesh for FEM and FVM.

Figure 10 – This figure illustrates the structured mesh used to analyze two discretization methods: (a) the finite element method and (b) the finite volume method.

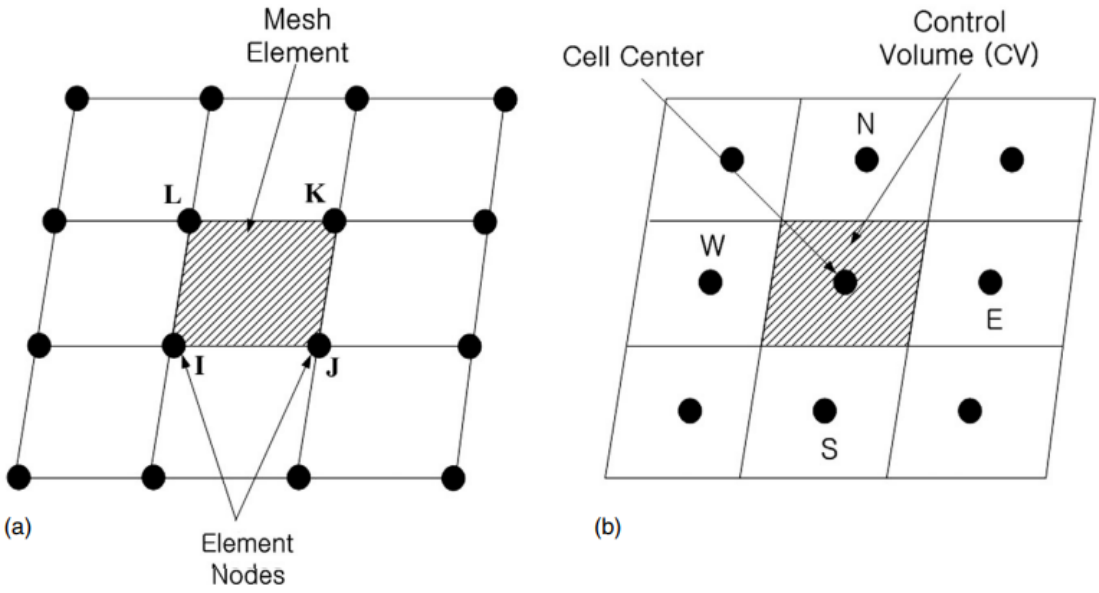


Source: Jeong and Seong (2014).

Boundary element method is used to solve certain classes of differential equations. The main advantage of this method is the fact that it only discretizes the domain contours while the others use the entire domain (CHAKRAVERTY *et al.*, 2019).

### *2.5.1 Element based Finite Volume Method*

The EbFVM intends to use the conservation principles directly in finite element ambient and emerged as its beginning applications in solving the Navier-Stokes equations together with unstructured meshes. The idea of the method is to have the properties conserved in discrete volumes around the mesh nodes. Thus, in EbFVM there is a control volume for each main node of mesh that is contained in sub-control volumes (CORDAZZO, 2006; FILIPPINI, 2011). Figure 11 illustrates the discretization of EbFVM.

Figure 11 – EbFVM discretization.

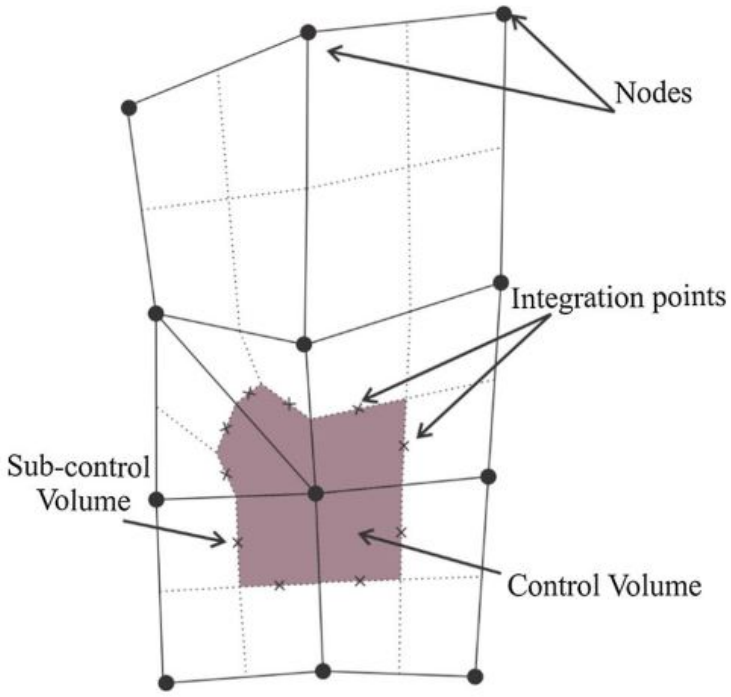


Source: Pimenta and Marcondes (2019).

EbFVM can be applied to Two Dimensions (2D) and Three Dimensions (3D) with unstructured meshes, this is due to the fact that the method has a more general and flexible approach in its discretization, as unstructured meshes have vertices with eventually variable local neighborhoods, offering a better convenience in mesh adaptation (BERN; PLASSMANN, 2000; XU *et al.*, 2020).

## 2.6 Machine learning

Machine learning is a rapidly growing field that brings together knowledge from several disciplines, including statistics, artificial intelligence, and computer science. The aim of machine learning is to develop algorithms that can learn from data, extract meaningful insights, and make predictions or decisions based on the patterns and relationships found in the data. There are two primary types of machine learning algorithms: supervised and unsupervised learning. In supervised learning, the algorithm is provided with labeled data, where the desired output is already known. By training on these data, the algorithm can learn to predict the correct output for new inputs. In contrast, unsupervised learning algorithms attempt to identify patterns and relationships within an unlabeled dataset without any predetermined output. This type of

learning is often used for exploratory analysis or to gain a deeper understanding of the data (MÜLLER; GUIDO, 2016; ALPAYDIN, 2009).

To be processed by machine learning algorithms, data must be converted into a format that computers can understand. Typically, data is organized into a table or matrix, with rows representing individual data samples and columns representing the different properties or features of those samples. The process of preparing data for machine learning is known as data preprocessing and involves tasks such as cleaning, normalization, and feature engineering. Supervised learning problems can be further divided into two categories: classification and regression. In classification problems, the algorithm predicts the category or label of a given input. If there are only two possible label options, it is known as binary classification, while problems with more than two possible labels are referred to as multiclass classification. Regression problems, on the other hand, involve predicting a continuous or numerical value, such as a price or temperature (MÜLLER; GUIDO, 2016; ALPAYDIN, 2009).

To ensure that machine learning models can generalize well to new, unseen data, it is essential to evaluate their performance on a separate test set. This can be achieved by splitting the available data into two sets: a training set, which is used to fit the model, and a test set, which is used to evaluate its performance. One commonly used method for splitting the data is called cross-validation. In this approach, the data is partitioned into several subsets, or "folds", and the model is trained and evaluated multiple times. The most popular form of cross-validation is k-fold cross-validation, where k is a user-defined parameter typically set to 5 or 10.

In k-fold cross-validation, the data is divided into k roughly equal parts, with each part being used once as a test set and the remaining k-1 parts used as the training set. The model is trained on the training set, and its performance is evaluated on the test set. This process is repeated k times, with each fold being used as the test set exactly once. Once all k iterations are complete, the performance of the model is summarized by calculating the average accuracy across all folds. This approach provides a more robust estimate of the model's performance on new data than a single train-test split, as it reduces the risk of overfitting to a particular training set. Additionally, k-fold cross-validation can help to optimize the model's hyperparameters, which are settings that affect the model's performance but are not learned from the data (MÜLLER; GUIDO, 2016). Figure 12 illustrates this division.

Figure 12 – Data splitting in five-fold cross-validation.

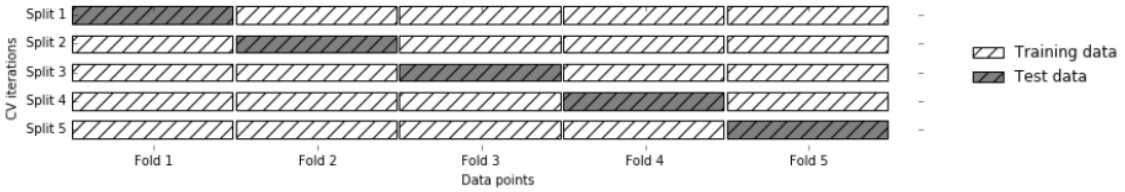


Source: Müller and Guido (2016).

When comparing this method to a simple random division, it is evident that it offers a range of advantages due to its ability to use data more effectively. By taking advantage of the inherent structure of the data, it is possible to derive insights and make more accurate predictions, which is particularly useful in applications where accuracy is of utmost importance. However, it is essential to consider the higher computational cost that comes with this method, which can be k times greater than that of the simplest case. Depending on the specific application, this may have a significant impact on the choice of method and should be carefully considered before proceeding.

To optimize the parameters of this method, a powerful technique called Grid Search can be utilized. Grid Search is a method within the scikit-learn library in Python that enables the testing of all possible combinations of hyperparameters that will be shown later and identifies the option with the best performance among those tested. This approach is particularly useful in situations where it is not clear which combination of parameters will result in the best performance, as it systematically tests each possible option to provide a comprehensive overview of performance. Additionally, Grid Search can be used in conjunction with cross-validation to evaluate the strengths and weaknesses of each methodology and to identify the optimal configuration for a given application (MÜLLER; GUIDO, 2016).

### *2.6.1 Deep learning*

During training, the neural network adjusts its parameters through a process called backpropagation, which involves passing the errors generated during each iteration of training back through the network. This allows the network to learn from its mistakes and adjust its internal weights and biases to improve its performance over time. However, it's important to note that there are other ways to update weights beyond backpropagation.

For example, some neural networks use reinforcement learning to adjust their parameters based on feedback from the environment, while others employ evolutionary algorithms

to optimize the weights and architecture of the network. Each of these methods has its own strengths and weaknesses, and the choice of which method to use will depend on the specific task and the characteristics of the data being analyzed. Figure 13 illustrates the structure of a neural network through a Multilayer Perceptron (MLP) (CORRIGAN, 2018).

Figure 13 – Structure of a neural network through a MLP.

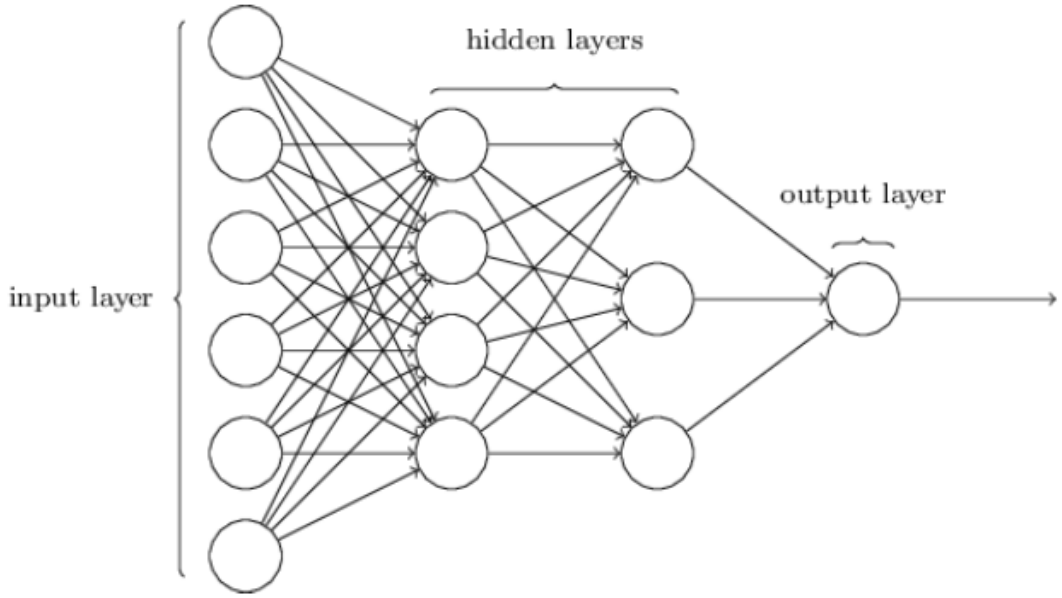


Source: Corrigan (2018).

Deep learning is a subarea of machine learning that uses multi-layered neural networks, with two or more hidden layers, in its architecture. Figure 14 shows a representation of this subarea. While this approach has seen tremendous advances in recent years, it's important to note that there are many other architectures that can be used as well, each with its own unique characteristics and capabilities (HEATON, 2015). Despite this challenge, the continuous advancements in hardware technology have made deep learning more accessible and practical for a wide range of applications.

Figure 14 – Subdivision of area of artificial intelligence.

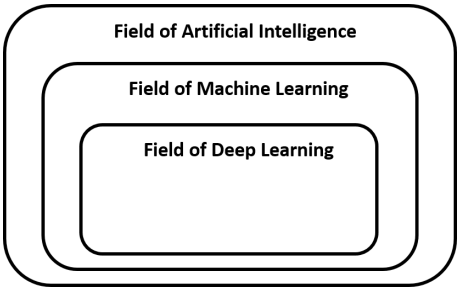


Source: Shinde and Shah (2019).

#### *2.6.1.1 Activation functions*

Activation functions play a crucial role in neural networks by introducing non-linearity to the model. They determine the output of a neuron or a layer and help the network learn complex relationships between inputs and outputs. Several activation functions have been proposed and used in different neural network architectures.

One of the commonly used activation functions is the sigmoid function, which maps the input to a value between 0 and 1 (RUMELHART *et al.*, 1986). The sigmoid function is given by:

$$f(x) = \frac{1}{1+e^{-x}} \tag{2.6}$$

The sigmoid function was widely used in earlier neural networks, but it has some limitations. One of the major issues is the vanishing gradient problem, where gradients become extremely small for inputs far from the origin, leading to slow learning. This limitation led to the development of alternative activation functions.

Another popular activation function is the Rectified Linear Unit (ReLU), which computes the output as zero for negative inputs and linear for positive inputs (GLOROT; BENGIO, 2010). ReLU has gained popularity due to its simplicity and ability to alleviate the vanishing gradient problem. However, ReLU suffers from a dying ReLU problem, where a large number of neurons may become inactive and never update their weights. This led to the development of variants such as Leaky ReLU and Parametric ReLU (PReLU). ReLU is defined as:

$$f(x) = max(0,x) \tag{2.7}$$

Other activation functions include the hyperbolic tangent (tanh) function, which maps inputs to a value between -1 and 1, and the softmax function, commonly used in the output layer for multi-class classification tasks (GOODFELLOW; COURVILLE, 2016).

A linear combiner is a fundamental component in artificial neural networks that combines the weighted input signals and a bias term to compute the net input of a neuron (RUMELHART *et al.*, 1986). The net input is then passed through an activation function to produce the neuron's output or activation. The linear combiner can be represented mathematically as follows:

$$y = f\left(\sum_{i=1}^{n} w_i x_i + b\right) \tag{2.8}$$

where:

- $y$ represents the output signal of the neuron,
- $f(\cdot)$ denotes the activation function,
- $w_i$ represents the synaptic weight associated with the input signal $x_i$,
- $b$ is the bias term, and
- $n$ represents the total number of input signals.

#### *2.6.1.2 Backpropagation algorithm*

The Backpropagation algorithm is a widely used technique in training artificial neural networks. It enables the network to learn from labeled training data and adjust its weights and biases to minimize the prediction error. This algorithm consists of two main phases: forward propagation and backward propagation.

During the forward propagation phase, input data is fed into the neural network, and the network's activation values are calculated layer by layer. Each neuron's activation is determined by applying an activation function to the weighted sum of its inputs, followed by passing it through a non-linear activation function. This process continues until the output layer is reached.

In the backward propagation phase, the error between the predicted output and the expected output is calculated. This error is then propagated back through the network, layer by layer, using the chain rule of calculus. The gradients of the weights and biases are computed with respect to the error, allowing for their adjustment. The weights and biases are updated using an optimization algorithm, such as stochastic gradient descent, which iteratively adjusts the parameters to minimize the error.

Backpropagation has been instrumental in the success of various neural network architectures, including multilayer perceptrons (MLPs) and Deep Neural Networks (DNNs). Its ability to efficiently train neural networks with multiple layers and non-linear activation functions has led to significant advancements in areas such as image recognition, natural language processing, and reinforcement learning.

Several seminal works have contributed to the development and understanding of the Backpropagation algorithm. Rumelhart *et al.* (1986) introduced Backpropagation in their influential paper, which outlined the basic principles and mathematical foundations of the algorithm. The paper demonstrated the effectiveness of Backpropagation in training multilayer neural networks.

Further advancements and refinements to the Backpropagation algorithm have been made over the years. LeCun *et al.* (2015) introduced Convolutional Neural Networks (CNNs) and made significant improvements to the Backpropagation algorithm for image classification tasks. Their work demonstrated the effectiveness of Backpropagation in deep learning applications.

#### *2.6.1.3 Hyperparameters*

Hyperparameters are parameters that are set before training and control the behavior and performanceof neural networks. These parameters are not learned during the training process but play a crucial role in determining the network's architecture and optimization process. Some commonly used hyperparameters in neural networks include:

- Learning rate: Determines the step size at each iteration of gradient descent. A high learning rate may cause the algorithm to overshoot the optimal solution, while a low learning rate may result in slow convergence. Choosing an appropriate learning rate is crucial for efficient and effective training (BOTTOU, 2012).
- Number of hidden layers: The depth of the network, i.e., the number of layers between the input and output layers. Deep networks have the potential to capture complex relationships but may be more prone to overfitting.
- Number of neurons per hidden layer: The number of neurons in each hidden layer. Increasing the number of neurons can increase the capacity of the network but may also lead to overfitting.
- Batch size: The number of training examples processed in each iteration of gradient descent. Larger batch sizes can result in faster training but may require more memory.
- Dropout rate: Dropout is a regularization technique that randomly sets a fraction of the activations to zero during training. It helps prevent overfitting by reducing the reliance on individual neurons and encourages the network to learn more robust representations (SRIVASTAVA *et al.*, 2014).
- Activation function: As discussed earlier, the choice of activation function can have a significant impact on the network's performance. Different activation functions may be more suitable for specific tasks or network architectures.
- Initialization of weights: The initial values assigned to the weights can affect how quickly the network converges and whether it gets stuck in local minima. Proper initialization techniques, such as Xavier or He initialization, can improve training performance (GLOROT;

BENGIO, 2010).

- Optimization algorithm: Gradient descent is the most commonly used optimization algorithm for updating the weights in neural networks. However, variations such as Stochastic Gradient Descent (SGD), Adam, or Root Mean Squared Propagation (RMSprop) can be used to enhance convergence speed and generalization (GOODFELLOW; COURVILLE, 2016).
- Early stopping: It involves monitoring the validation loss during training and stopping the training process when the validation loss starts to increase. This helps prevent overfitting and ensures that the network is not trained for too long.

These are just a few examples of hyperparameters used in neural networks. The choice of hyperparameters depends on the specific problem, dataset, and network architecture. It often requires experimentation and fine-tuning to find the optimal set of hyperparameters for a given task.

The process of selecting hyperparameters is often iterative and involves techniques such as grid search, random search, or more advanced methods like Bayesian optimization. Careful tuning and experimentation with different hyperparameter configurations are necessary to find the optimal settings for a specific task.

# 3 NUMERICAL SIMULATION OF THERMAL BEHAVIOR IN TIG WELDING WITH AUSTENITIC STAINLESS STEELS USING EBFVM

## 3.1 Review

This work analyzed the thermal behavior of autogenous TIG welding process in plates with austenitic stainless steels (316L, 316 and 304) using numerical simulation with EbFVM, comparing the simulated temperature distributions with the temperatures found in experimental cases in the literature. Experimental case studies were collected from the literature and used to investigate and validate this phenomenon. The numerical process was developed in Fortran language applying the numerical method EbFVM. The numerical-experimental comparison was made both qualitatively, through the graphs of thermal cycles, and quantitatively, through the performance indices (MAPE and CV). The spatial and temporal refinements used in the simulation were investigated to understand the influence of each of these factors on thermal behavior. With the numerical validation of these experimental cases, predictions of thermal cycles and maximum temperatures of possible welding configurations were performed. In addition, a study on the computational cost of these simulations was carried out. This used methodology proved to be efficient in the analysis of thermal behavior of this welding process applied to these materials.

## 3.2 Materials and methods

### *3.2.1 Numerical welding modeling*

The TIG welding process can be modeled from the heat energy that is diffused into the workpiece. This heat transfer can be understood through a general thermal analysis considering the fundamental phenomena of conduction, convection, and radiation. For this case, some hypotheses can be assumed seeking to simplify the computational costs, keeping the modeled process close to the real one. It is assumed that the welded material is at rest in relation to the welding source and that the thermal properties of the material are constant in the directions of chosen coordinate system. Thus, based on the Cartesian coordinate system, the process can be represented through the heat energy governing equation as a function of temperature $T(x,y,z,t)$ (GUR; PAN, 2008):

$$\frac{\partial}{\partial x}\left(k(T)\frac{\partial T}{\partial x}\right)+\frac{\partial}{\partial y}\left(k(T)\frac{\partial T}{\partial y}\right)+\frac{\partial}{\partial z}\left(k(T)\frac{\partial T}{\partial z}\right)+Q(x,y,z,t)=\rho(T)c_p(T)\frac{\partial T}{\partial t}, \tag{3.1}$$

with,

$k$ - thermal conductivity $[Wm^{-1}K^{-1}]$,

$\rho$ - density $[kg\ m^{-3}]$,

$c_p$ - heat capacity $[J\ kg^{-1}K^{-1}]$,

$Q$ - intensity of heat source $[Wm^{-3}]$.

The boundary conditions for this equation relate the heat exchanges that occur for this welding process. The natural boundary condition relates the heat transfer coefficient between the workpiece and the ambient area through the equation below:

$$-k_n \frac{\partial T}{\partial n} = h_g(T_\infty - T_s) \tag{3.2}$$

with,

$k_n$ - thermal conductivity normal to the surface $[Wm^{-1}K^{-1}]$,

$\partial T/\partial n$ - temperature gradient on the boundary along the external normal direction $[Km^{-1}]$,

$h_g$ - global heat transfer coefficient $[Wm^{-2}K^{-1}]$,

$T_\infty$ - ambient temperature $[K]$,

$T_s$ - surface temperature $[K]$.

The global heat transfer coefficient can be divided as a function of convection and radiation coefficients:

$$h_g = h_c + h_r \tag{3.3}$$

with,

$h_c$ - heat transfer coefficient for convection $[Wm^{-2}K^{-1}]$,

$h_r$ - heat transfer coefficient for radiation $[Wm^{-2}K^{-1}]$,

in which,

$$h_r = \varepsilon\sigma(T_\infty^2 + T_s^2)(T_\infty + T_s) \tag{3.4}$$

with,

$\varepsilon$ - emissivity,

$\sigma$ - Stefan-Boltzmann constant $[Wm^{-2}K^{-4}]$.

The initial temperature was considered to be to equal the ambient temperature of the area where welding takes place and the fluid flow in the molten weld pool hasn't been considered. Figure 15 shows the arrangement of the process on rectangular plates, illustrating the path and

direction of welding, the heat source, the melting pool generated, and the adopted coordinate system.

Figure 15 – Arrangement of welding process on rectangular plates.

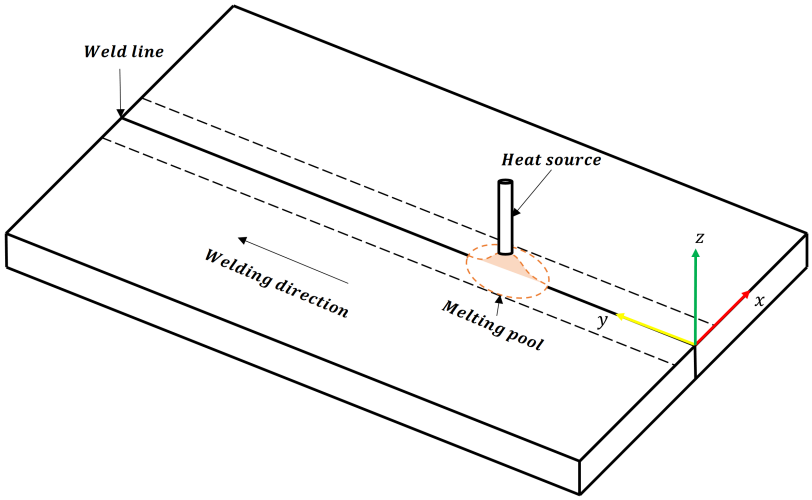


Source: Own author.

The heat source term can be calculated from a model among those already existing in the literature. However, new models are continually being studied and validated, seeking to better represent the behavior of heat sources. According to Goldak and Akhlaghi (2005), the most used model for welding heat input is the double ellipsoidal one, coming from the second generation of source models. It is a Gaussian power density distribution within a double ellipsoidal moving along the weld. This model has a good approximation, convenient, accurate, and efficient for the TIG welding process, as it reflects the depth and the generated shapes. Therefore, this methodology is chosen to be used for this study. Malik *et al.* (2008) adapted the equations of this volumetric method as a function of the cartesian coordinate system $(x, y, z)$:

$$Q_f(x,y,z,t) = \frac{6\sqrt{3} f_f S}{a_f bc\pi\sqrt{\pi}} e^{(-3x^2/a_f^2)} e^{(-3y^2/b^2)} e^{(-3z^2/c^2)} \tag{3.5}$$

$$Q_r(x,y,z,t) = \frac{6\sqrt{3} f_r S}{a_r bc\pi\sqrt{\pi}} e^{(-3x^2/a_r^2)} e^{(-3y^2/b^2)} e^{(-3z^2/c^2)} \tag{3.6}$$

with,

$a_f$ - length of front ellipsoidal $[m]$,

$a_r$ - length of rear ellipsoidal $[m]$,

$f_f$ - fraction of heat in front ellipsoidal,

$f_r$ - fraction of heat in rear ellipsoidal,

$S$ - total heat input $[W]$,

$b$ - half-width of heat source $[m]$,

$c$ - depth of heat source $[m]$,

$Q_f$ - power density in front ellipsoidal $[Wm^{-3}]$,

$Q_r$ - power density in rear ellipsoidal $[Wm^{-3}]$.

In which $S = \eta EI$ e $f_f + f_r = 2$, with $\eta$ being the arc efficiency, $E$ the welding voltage $[V]$ and $I$ the welding current $[A]$. Figure 16 show the double ellipsoidal heat source with the parameters needed in modeling.

Figure 16 – Double ellipsoidal heat source.

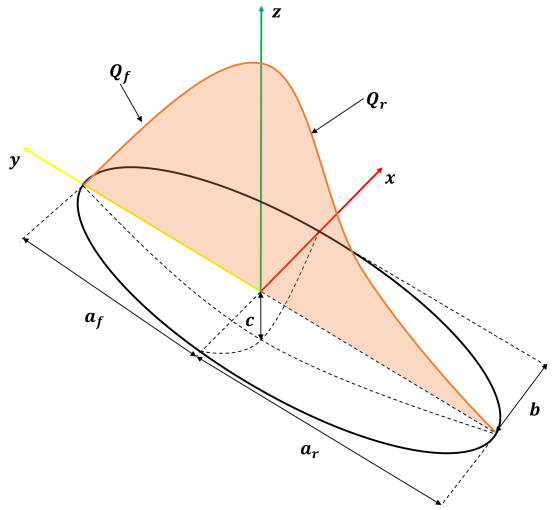


Source: Own author.

### *3.2.2 Welding cases*

Based on the modeling developed for the welding process, experimental data were searched in the literature to validate and measure the performance of this methodology. Four cases were selected that use the autogenous TIG process with only one step to weld austenitic stainless steel plates. Table 2 shows the main characteristics used in experimental case studies, such as the type of material, plate geometry, welding parameters (voltage $E$, current $I$, welding velocity $v_w$ and efficiency $\eta$), the ambient temperature $T_\infty$ and the source of research.

Table 2 – Main features of case studies.

| Case | Material | Geometry $[mm^3]$ | E $[V]$ | I $[A]$ | $v_w$ $[mms^{-1}]$ | $\eta$ | $T_\infty$ $[K]$ | Source |
|---|---|---|---|---|---|---|---|---|
| Case 01 | 316L | 250 x 160 x 10 | 10.0 | 150 | 1.0 | 0.68 | 302 | (CARMO; FARIA, 2015) (DEPRADEUX, 2004) |
| Case 02 | 316 | 110 x 60 x 10 | 16.3 | 306 | 7.98 | 0.80 | 298 | (SILVA *et al.*, 2020) |
| Case 03 | 304 | 200 x 100 x 2 | 10.0 | 100 | 10.0 | 0.70 | 300 | (JOO *et al.*, 2016) |
| Case 04 | 304 | 150 x 75 x 3 | 24.0 | 100 | 2.44 | 0.60 | 313 | (VENKATKUMAR; RAVINDRAN, 2016) |

Source: Own author.

Table 3 shows the necessary properties, as a function of temperature, for simulation with the steels used in four case studies (product between density and heat capacity $\rho c_p$ and thermal conductivity $k$). The chosen temperatures seek to take better advantage of intervals found between the case studies, however, temperatures are added that cover the range in which the phase transformations of these steels occur (MIYATA *et al.*, 2021; MUKHERJEE *et al.*, 2017). The values of properties not provided in these experimental works were interpolated to maintain the same temperature range ($273K - 1773K$) in all case studies.

Table 3 – Material properties of case studies.

| Case | Case 01 | | Case 02 | | Case 03-04 | |
|---|---|---|---|---|---|---|
| $T$ $[K]$ | $\rho c_p$ $[Jm^{-3}K^{-1}]$ | $k$ $[Wm^{-1}K^{-1}]$ | $\rho c_p$ $[Jm^{-3}K^{-1}]$ | $k$ $[Wm^{-1}K^{-1}]$ | $\rho c_p$ $[Jm^{-3}K^{-1}]$ | $k$ $[Wm^{-1}K^{-1}]$ |
| 273.0 | 4593000.0 | 13.48 | 4153504.0 | 27.78 | 3649800.0 | 14.60 |
| 373.0 | 4593000.0 | 14.92 | 4248304.0 | 28.58 | 3908480.0 | 15.10 |
| 473.0 | 4593000.0 | 16.36 | 4343104.0 | 29.38 | 4008960.0 | 16.10 |
| 573.0 | 4593000.0 | 17.80 | 4437904.0 | 30.18 | 4089750.0 | 17.90 |
| 673.0 | 4593000.0 | 19.23 | 4532704.0 | 30.98 | 4185000.0 | 18.00 |
| 873.0 | 4593000.0 | 22.11 | 4722304.0 | 32.58 | 4419820.0 | 20.80 |
| 1073.0 | 4593000.0 | 24.98 | 4911904.0 | 34.18 | 4566240.0 | 23.90 |
| 1473.0 | 4593000.0 | 30.73 | 5291104.0 | 37.38 | 4982120.0 | 32.20 |
| 1573.0 | 4593000.0 | 32.17 | 5385904.0 | 38.18 | 5065440.0 | 33.70 |
| 1673.0 | 29810000.0 | 47.57 | 5480704.0 | 38.98 | 5094720.0 | 76.85 |
| 1773.0 | 4927000.0 | 60.00 | 5575504.0 | 39.78 | 5124000.0 | 120.0 |

Source: Own author.

Table 4 shows the global heat transfer coefficient $h_g$ as a function of temperature. For Case 01, the coefficient calculation considers only convection, ignoring radiation, but in other cases, both phenomena are included. According to this case study 01, some properties were considered constant. For Case 02, the calculation is performed using the Equations 3.3 and 3.4. In Cases 03 and 04, they use a set of equations according to the defined temperature intervals.

Table 4 – Global heat transfer coefficient of case studies.

| Case | Case 01 | Case 02 | Case 03 | Case 04 |
|---|---|---|---|---|
| $T$ $[K]$ | $h_g$ $[Wm^{-2}K^{-1}]$ | | | |
| 273.0 | 10.000 | 18.606 | 0.000 | 18.236 |
| 373.0 | 10.000 | 20.914 | 6.680 | 24.916 |
| 473.0 | 10.000 | 24.318 | 13.360 | 31.596 |
| 573.0 | 10.000 | 29.049 | 20.040 | 38.276 |
| 673.0 | 10.000 | 35.341 | 26.720 | 44.956 |
| 873.0 | 10.000 | 53.532 | 56.500 | 119.563 |
| 1073.0 | 10.000 | 80.747 | 102.700 | 165.763 |
| 1473.0 | 10.000 | 169.672 | 195.100 | 258.163 |
| 1573.0 | 10.000 | 200.444 | 218.200 | 281.263 |
| 1673.0 | 10.000 | 235.095 | 241.300 | 304.363 |
| 1773.0 | 10.000 | 273.859 | 264.400 | 327.463 |

Source: Own author.

### *3.2.3 Simulations*

After the process modeling and the selection of experimental cases in the literature, a computational code in Fortran developed jointly with the members of the Computational Fluid Dynamics Laboratory (LDFC), was modified using 3D hexahedron elements and an implicit formulation with EbFVM to solve this non-linear transient problem. Only the symmetrical half (in relation to the weld bead) of the plate was used in the approach, seeking to reduce computational costs. This procedure doesn't affect the final result and reduces the calculation performed by a computer. The grid used in simulations was designed in ICEM Computational Fluid Dynamics (CFD) tool of ANSYS software. In the same tool, with the developed geometry, the meshes defined for this study were generated. For this, the code was created with a function that reads the mesh files generated in the pattern provided by this software.

To better organize the results, the cases under study were divided according to the positions on the plate where the experimental data were collected, together with the final time of the thermal cycle. Table 5 illustrates this division. For all cases, the total time of thermal cycles used in experimental work was used, except for Case 04, which was reduced to 400$s$ as it would be enough to understand the behavior.

Table 5 – Division of case studies.

| Cases | Label | Cycle time [$s$] | Position | | |
|---|---|---|---|---|---|
| | | | $x$ [$mm$] | $y$ [$mm$] | $z$ [$mm$] |
| Case 01 | C01-E01 | 400 | 10.0 | 95.0 | 10.0 |
| | C01-E02 | 400 | 20.0 | 95.0 | 10.0 |
| | C01-E03 | 400 | 50.0 | 95.0 | 10.0 |
| | C01-E04 | 400 | 0.0 | 95.0 | 0.0 |
| | C01-E05 | 400 | 8.0 | 95.0 | 0.0 |
| | C01-E06 | 400 | 20.0 | 95.0 | 0.0 |
| | C01-E07 | 400 | 35.0 | 95.0 | 0.0 |
| Case 02 | C02-E01 | 70 | 0.0 | 55.0 | 5.0 |
| Case 03 | C03-E01 | 300 | 0.0 | 100.0 | 0.0 |
| | C03-E02 | 300 | 5.0 | 100.0 | 0.0 |
| | C03-E03 | 300 | 10.0 | 100.0 | 0.0 |
| | C03-E04 | 300 | 16.0 | 100.0 | 0.0 |
| | C03-E05 | 300 | 24.0 | 100.0 | 0.0 |
| | C03-E06 | 300 | 32.0 | 100.0 | 0.0 |
| | C03-E07 | 300 | 40.0 | 100.0 | 0.0 |
| Case 04 | C04-E01 | 400 | 9.5 | 47.5 | 3.0 |
| | C04-E02 | 400 | 7.5 | 75.0 | 3.0 |
| | C04-E03 | 400 | 7.5 | 102.5 | 3.0 |

Source: Own author.

For performing all these simulations, a computational cluster composed of a headnode with computational nodes having two types of servers was used. Headnode has two Intel Xeon E5-2630 v4 2.2GHz processors, 64GB DDR3 1866Mhz ECC RAM and five 8TB SAS HDDs in RAID 5. The first type of compute node has two Intel Xeon E5-2630 v4 2.2GHz processors, 64GB DDR3 RAM 1866Mhz ECC, and a 1TB SATA HDD. The second type has two Intel Xeon X5660 2.8GHz processors, 48GB RAM, and a 500GB HDD. This equipment was made available by the Computational Fluid Dynamics Laboratory (LDFC) which is located in the Department of Metallurgical and Materials Engineering at Federal University of Ceará (UFC).

In order to obtain the best results, close to those found in literature, the four defined cases were simulated several times, varying the parameters of the heat source with a time-step equal to $\Delta t = 1.0s$. Table 6 shows the parameters of the heat source that presented the best performance for these cases under study.

Table 6 – Parameters of heat source of case studies.

| Case | Heat source parameters | | | | | |
|---|---|---|---|---|---|---|
| | $a_f$ $[mm]$ | $a_r$ $[mm]$ | $b$ $[mm]$ | $c$ $[mm]$ | $f_f$ | $f_r$ |
| Case 01 | 6.0 | 6.0 | 6.0 | 6.0 | 1.4 | 0.6 |
| Case 02 | 10.0 | 1.0 | 3.5 | 10.0 | 1.6 | 0.4 |
| Case 03 | 8.0 | 12.0 | 5.0 | 2.0 | 0.8 | 1.2 |
| Case 04 | 10.0 | 16.0 | 3.0 | 10.0 | 1.4 | 0.6 |

Source: Own author.

With these parameters defined, a refinement study was made in time and space. The following time-step $\Delta t$ were used: $0.25s$, $0.50s$, $1.0s$ to understand the behavior of the solution with a greater division of steps. The sizes in mesh refinement were defined in order to reduce the size of elements close to the weld bead. In addition, an attempt was made to match the position of points collected experimentally in the case of studies, in positions of nodes of generated meshes, to facilitate comparisons. Table 7 shows the number of elements and nodes of each mesh generated under investigation.

Table 7 – Mesh refinement of case studies.

| Case | Mesh | Elements | Nodes |
|---|---|---|---|
| Case 01 | R01 | 1600 | 2601 |
| | R02 | 6000 | 9333 |
| | R03 | 15000 | 18666 |
| Case 02 | R01 | 440 | 759 |
| | R02 | 6600 | 10323 |
| | R03 | 13200 | 17205 |
| Case 03 | R01 | 2000 | 3198 |
| | R02 | 9000 | 13938 |
| | R03 | 18000 | 23230 |
| Case 04 | R01 | 3480 | 5490 |
| | R02 | 6960 | 9150 |
| | R03 | 13688 | 21330 |

Source: Own author.

In addition, simulations were performed seeking to estimate and predict the behavior of these cases in different situations with other values of current, voltage, and welding efficiency, keeping the welding process velocity, geometry, and thermal properties. The predicted values were collected from the central point of the plate in the upper region with the source parameters, and with the temporal and spatial refinements that performed better with Average MAPE ($MAPE_m$) in experimental case studies. Table 8 shows how these simulations were organized.

Table 8 – Division the predictions of each cases under study.

| Case | Label | Cycle time [$s$] | Welding parameters | | | | Position | | |
|---|---|---|---|---|---|---|---|---|---|
| | | | $E$ [$V$] | $I$ [$A$] | $\eta$ | $v_w$ [$mms^{-1}$] | $x$ [$mm$] | $y$ [$mm$] | $z$ [$mm$] |
| Case 01 | C01-P01 | 400 | 10.0 | 150 | 0.68 | 1.0 | 0 | 125 | 10 |
| | C01-P02 | 400 | 16.3 | 306 | 0.80 | 1.0 | 0 | 125 | 10 |
| | C01-P03 | 400 | 10.0 | 100 | 0.70 | 1.0 | 0 | 125 | 10 |
| | C01-P04 | 400 | 24.0 | 100 | 0.60 | 1.0 | 0 | 125 | 10 |
| Case 02 | C02-P01 | 70 | 16.3 | 306 | 0.80 | 7.98 | 0 | 55 | 10 |
| | C02-P02 | 70 | 10.0 | 150 | 0.68 | 7.98 | 0 | 55 | 10 |
| | C02-P03 | 70 | 10.0 | 100 | 0.70 | 7.98 | 0 | 55 | 10 |
| | C02-P04 | 70 | 24.0 | 100 | 0.60 | 7.98 | 0 | 55 | 10 |
| Case 03 | C03-P01 | 300 | 10.0 | 100 | 0.70 | 10.0 | 0 | 100 | 2 |
| | C03-P02 | 300 | 10.0 | 150 | 0.68 | 10.0 | 0 | 100 | 2 |
| | C03-P03 | 300 | 16.3 | 306 | 0.80 | 10.0 | 0 | 100 | 2 |
| | C03-P04 | 300 | 24.0 | 100 | 0.60 | 10.0 | 0 | 100 | 2 |
| Case 04 | C04-P01 | 400 | 24.0 | 100 | 0.60 | 2.44 | 0 | 75 | 3 |
| | C04-P02 | 400 | 10.0 | 100 | 0.70 | 2.44 | 0 | 75 | 3 |
| | C04-P03 | 400 | 10.0 | 150 | 0.68 | 2.44 | 0 | 75 | 3 |
| | C04-P04 | 400 | 16.3 | 306 | 0.80 | 2.44 | 0 | 75 | 3 |

Source: Own author.

### *3.2.4 Performance of numerical simulations*

To compare the numerical results with those collected experimentally in case studies, statistical metrics were used to help measure the performance of each simulation. The Mean Absolute Percentage Error (MAPE) metric is an excellent quantitative indicator that is widely used to check errors between actual values and predictions (GUIMARÃES, 2020). For this case, the $MAPE$ [%] is calculated using the following equation (ANSARI *et al.*, 2018):

$$MAPE = \sum_{i=1}^{n} \frac{1}{n} \frac{|T_i^e - T_i^s|}{T_i^e} \times 100 \tag{3.7}$$

where:

$T_i^e$ - temperatures collected in each experimental thermal cycle [$K$],

$T_i^s$ - temperatures collected in each simulated thermal cycle [$K$],

$n$ - number of points of each thermal cycle.

Since in most of these case studies, there is more than one point collected experimentally, then a mean of MAPE of the thermal cycle of each point is performed. In addition, to verify and compare the refinements used in the same case, the Coefficient of Variation $CV$ was used. This measure of dispersion shows how homogeneous the set of errors is within the same case, as it relates the variability of data (standard deviation) with the magnitude of its mean.(FAVERO; BELFIORE, 2019). The $CV$ is calculated this case using the following equation (HEUMANN;

SCHOMAKER, 2017):

$$CV = \frac{s}{MAPE_m} \tag{3.8}$$

with,

$$s = \sqrt{\sum_{i=1}^{n} \frac{(MAPE_i - MAPE_m)^2}{n}} \tag{3.9}$$

and $MAPE_m$ is a mean of $MAPE$ values.

Finally, to compare the computational costs of simulations performed, the total Central Processing Unit (CPU) time $t_{CPU}$ in seconds was used.

## 3.3 Results

With all the simulations performed, it was possible to compare the results of performance metrics. Figure 17 illustrates the $MAPE_m$ for all cases for the different mesh refinements and time steps.

Figure 17 – Mean values of $MAPE$ in cases under study.

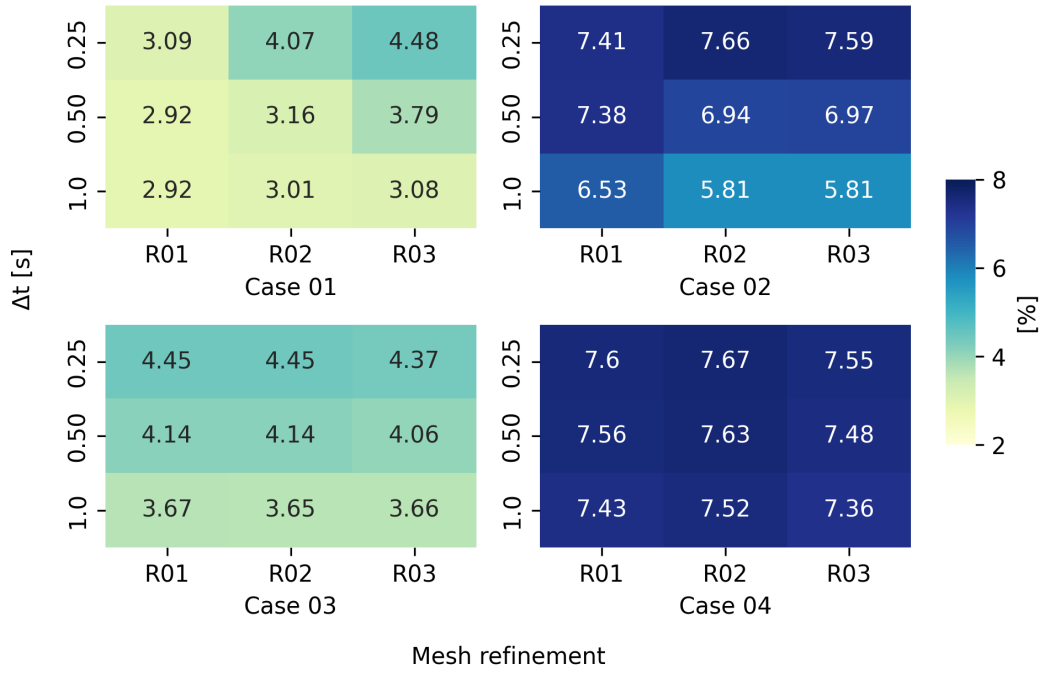


Source: Own author.

It can be seen that in Case 01 it had the lowest value of $MAPE_m$ among all cases, with 2.92%, in which it used a mesh with 1600 elements and $\Delta t = 1.0s$. For this case, there was an increase in metric with a greater refinement of mesh or with a decrease in a time interval.

This increase can be considered irrelevant since the differences are small and can be attributed to some approximations. For Case 02, the best value was 5.81% using a mesh of 6600 elements and with a time-step of 1.0$s$. For Case 02, there was a behavior similar to Case 01 when temporal refinement is performed. However, there is a decrease of $MAPE_m$ with spatial refinement in most configurations for Case 02. For Case 03, the lowest value was 3.66% with 18000 elements in mesh and $\Delta t = 1.0s$. However, there was a decrease in metric with mesh refinement and an increase with decreasing time intervals. Finally, for Case 04, we had the highest value of $MAPE_m$ among all the lowest in other cases, with 7.36%, using a mesh of 13688 elements and an interval of 1.0$s$. The same behavior of Case 03 with the refinement of time intervals occurs for this case, however in mesh refinement from R01 to R02 there is an increase, and from R02 to R03 there is a decrease.

The same analysis was performed by comparing the CV values in which it was possible to visualize the homogeneity of errors. Figure 18 shows this comparison for the cases, except Case 02 because it has zero variability, having only a single experimental collection point.

Figure 18 – CV values in cases under study.

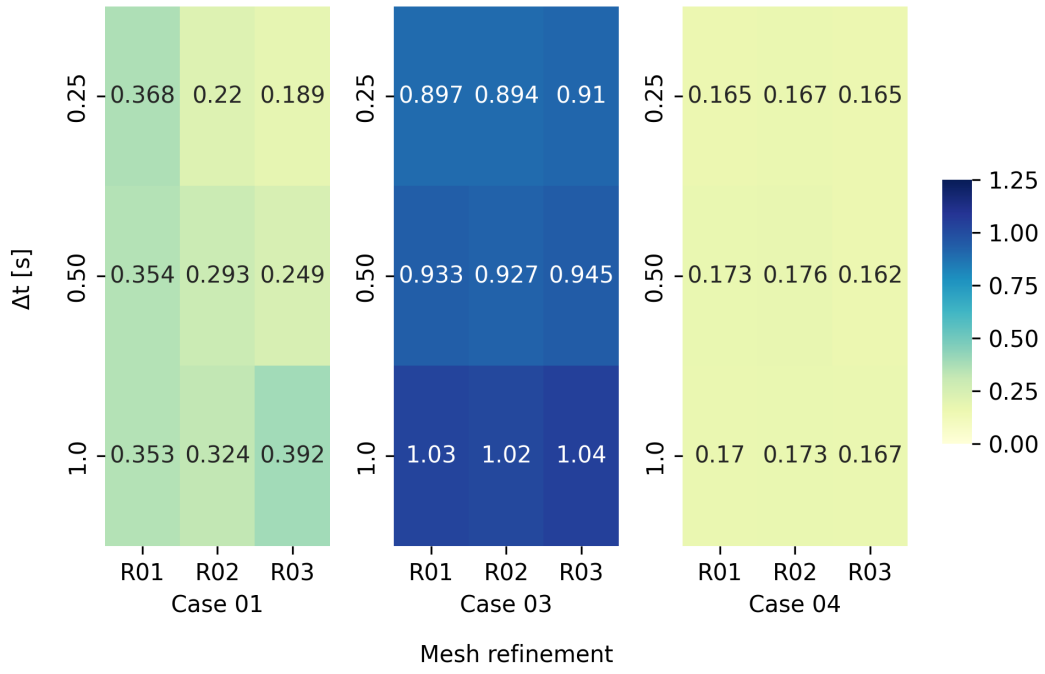


Source: Own author.

For Case 01, the smallest CV value was 0.189 when it was simulated with a mesh of 15000 elements and with $\Delta t = 0.25s$. With the refinement of mesh and the time interval, it was noticed, in general, a more homogeneous behavior. The value of 0.894 was the lowest found

in Case 03, using a mesh of 9000 elements and with $\Delta t = 0.25s$. The best values for this case with mesh refinement occurred with type R02. In addition, the decrease in time-step resulted in a greater homogeneity of errors for this case. Finally, in Case 04, the lowest CV value was found among all cases, with 0.162 when a mesh of 13688 elements was used and $\Delta t = 0.50s$. The extreme values in this case were very close with a maximum relative absolute difference of 8.64%. The highest value of Case 04 is smaller than all the others of other cases. However, more homogeneous data was obtained when passing from the refinement R01 to R03 and from the time interval $1.0s$ to $0.25s$ directly, without going through the intermediate refinement layer.

Figure 19 illustrate the mesh generated for case 01 with the refinement 01 that was used in simulations, in which it is possible to visualize the type of refinement performed for this case in three Cartesian directions, for example.

Figure 19 – Generated mesh - Case 01 - R01.

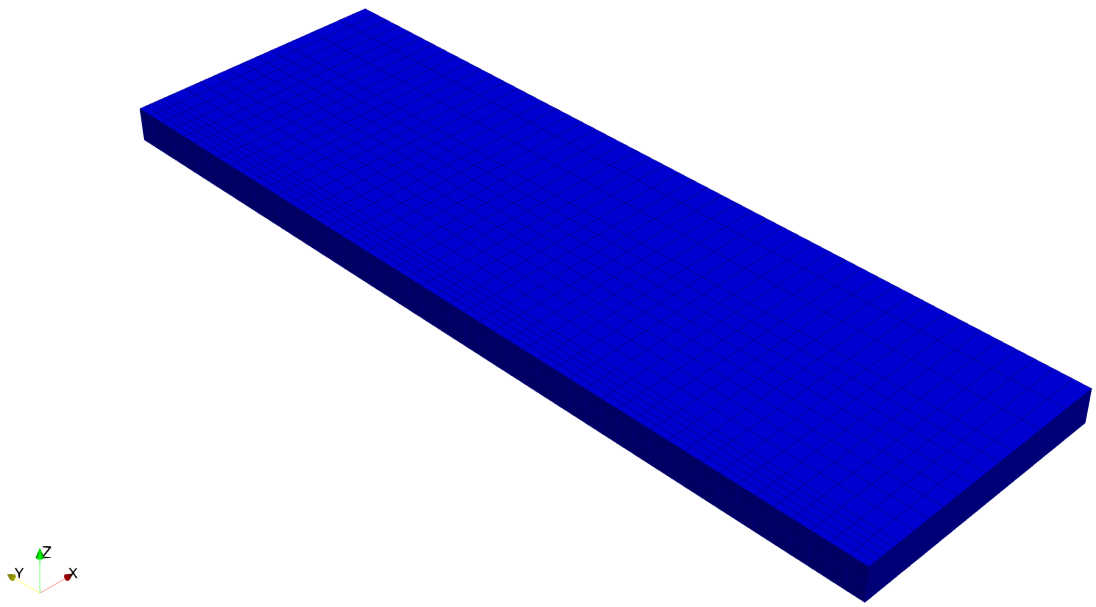


Source: Own author.

The thermal cycle results obtained with the best $MAPE_m$ can be seen in Figures 20-23 and with the best $CV$ in Figures 24-26, together with the data collected experimentally for

each case.

Figure 20 – Numerical-experimental comparison - Best $MAPE_m$ - Case 01 - R01 - $\Delta t = 1.0s$.

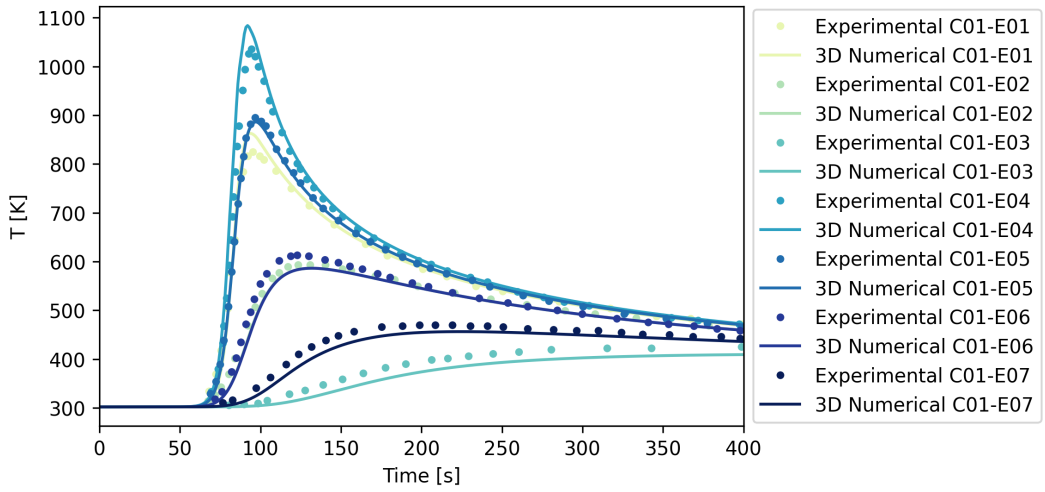


Source: Own author.

Figure 21 – Numerical-experimental comparison - Best $MAPE_m$ - Case 02 - R02 - $\Delta t = 1.0s$.

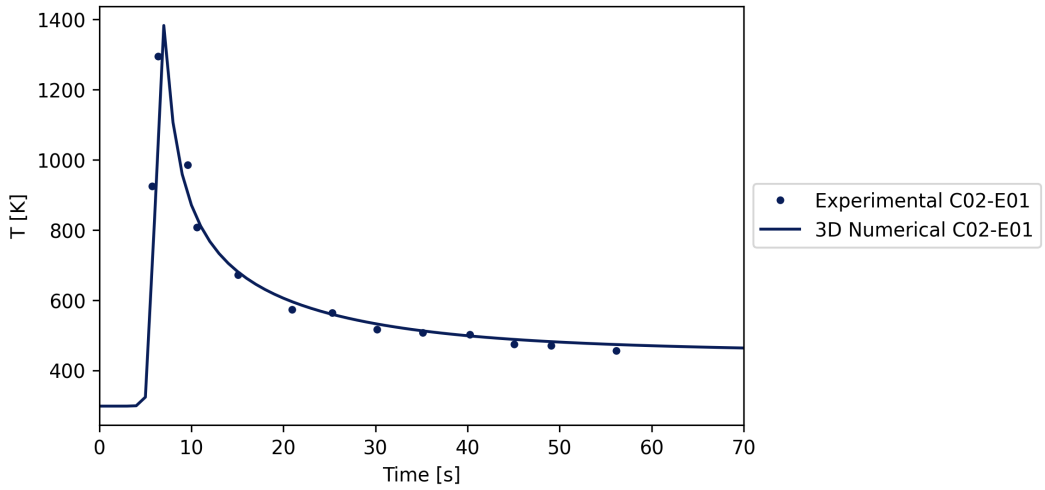


Source: Own author.

Figure 22 – Numerical-experimental comparison - Best $MAPE_m$ - Case 03 - R02 - $\Delta t = 1.0s$.

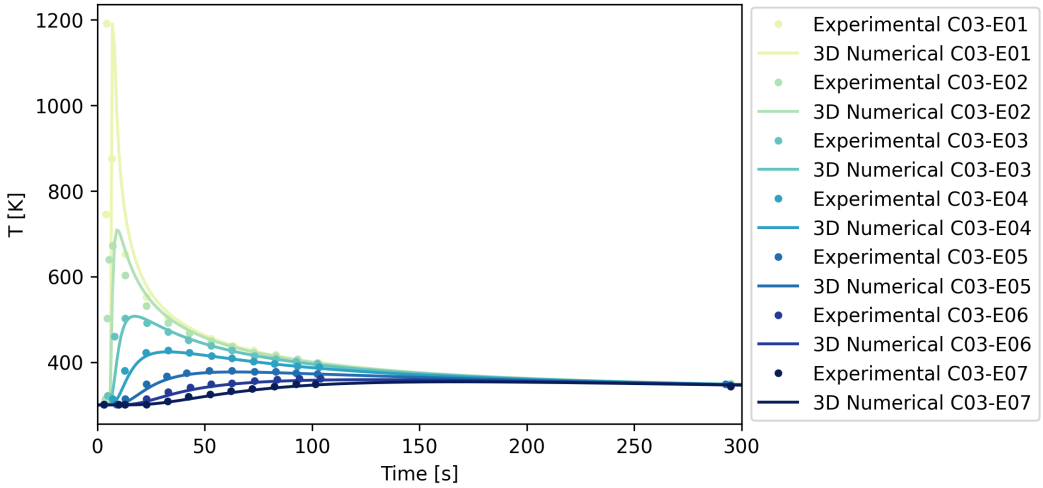


Source: Own author.

Figure 23 – Numerical-experimental comparison - Best $MAPE_m$ - Case 04 - R03 - $\Delta t = 1.0s$.

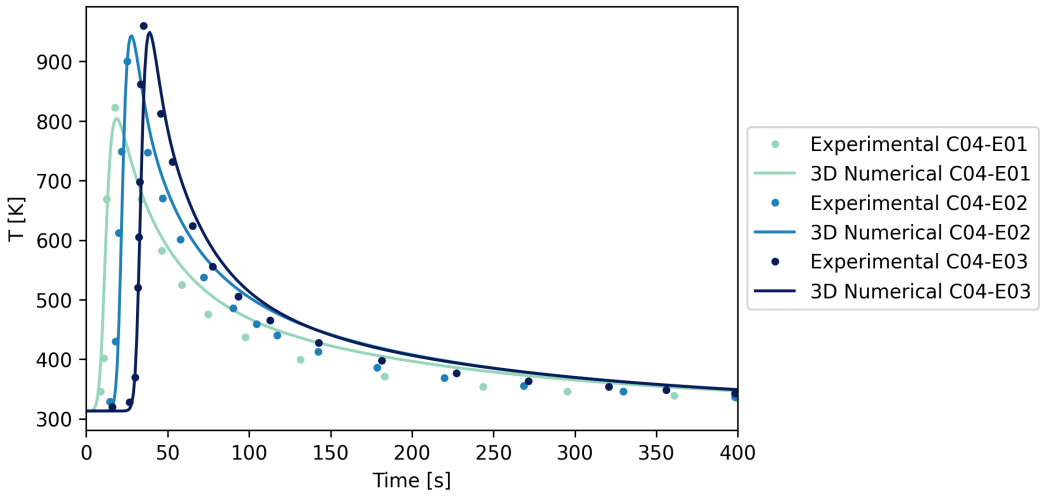


Source: Own author.

Figure 24 – Numerical-experimental comparison - Best *CV* - Case 01 - R03 - $\Delta t = 0.25s$.

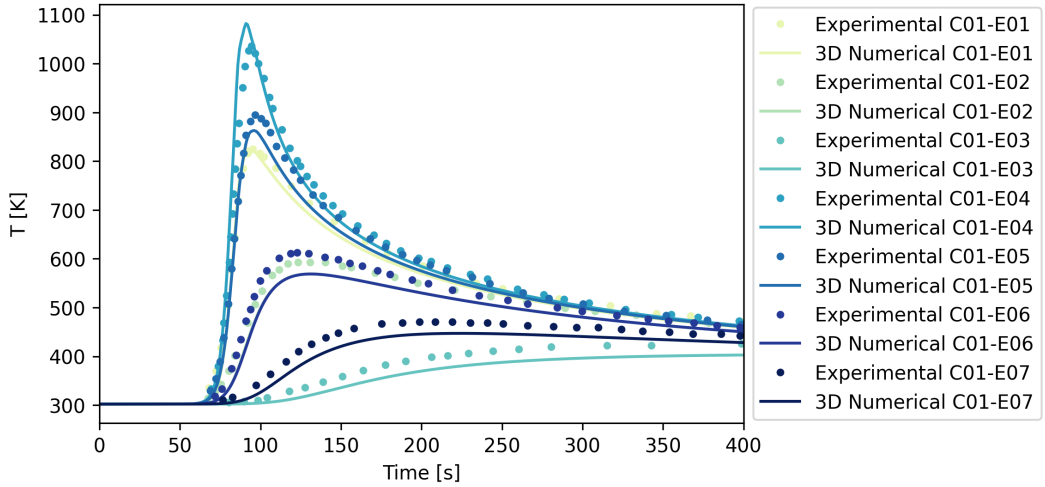


Source: Own author.

Figure 25 – Numerical-experimental comparison - Best *CV* - Case 03 - R02 - $\Delta t = 0.25s$.

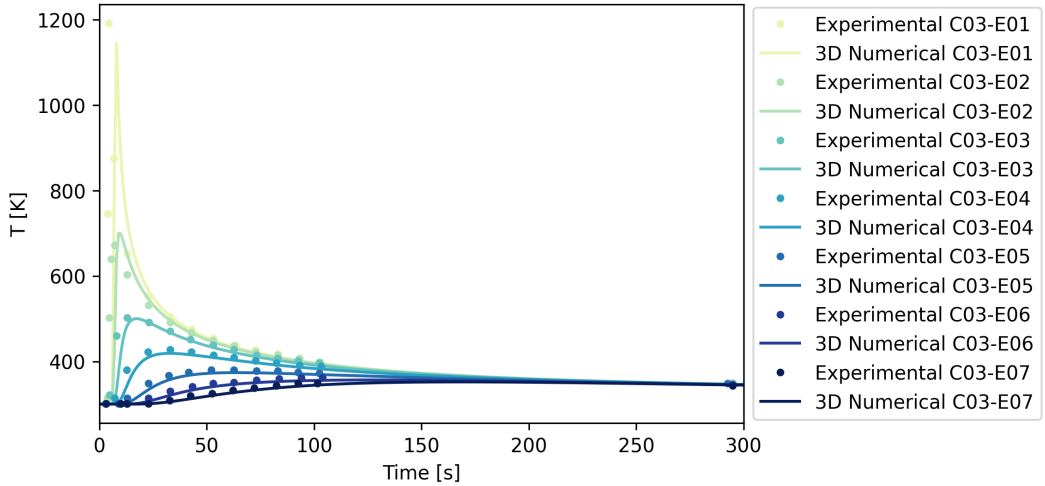


Source: Own author.

Figure 26 – Numerical-experimental comparison - Best $CV$ - Case 04 - R03 - $\Delta t = 0.50s$.

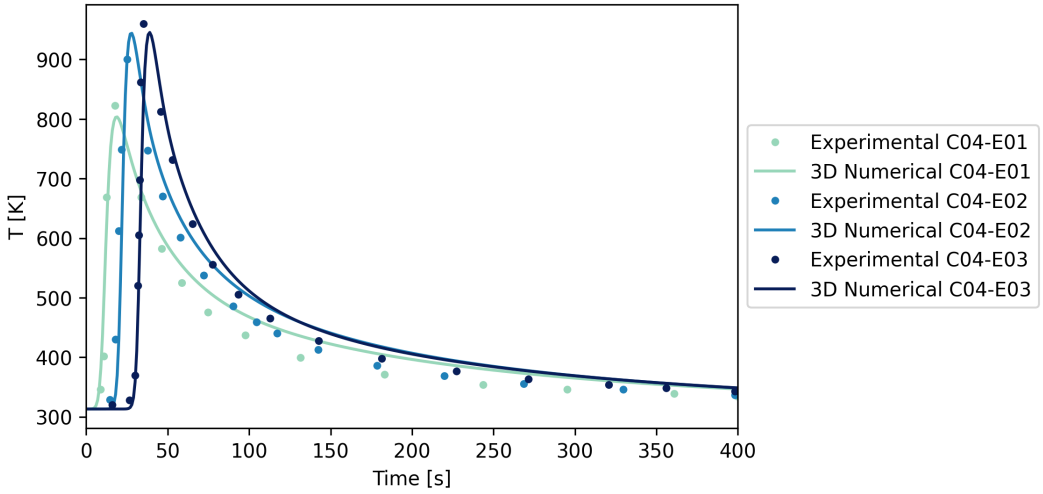


Source: Own author.

It can be seen that the numerical results of thermal cycles were close to those found experimentally for the four cases, both for the best values of $MAPE_m$ and for the greater homogeneity given by $CV$, showing the efficiency of the adopted methodology. The temperature peaks of the cycles are consistent with the allocated positions on the plate, being smaller in positions further away from the heat source and greater the closer the heat source. Values consistent with the experimental cases under study. In addition to these graphs, it was possible to compare the maximum temperatures obtained in simulations. The temperature value found for the best $MAPE_m$ was used as a reference to calculate the relative difference between the maximum temperature values. Table 9 shows these values.

Table 9 – Maximum temperatures in cases under study.

| Case | Label | MAPE[Ref.] | CV | Relative difference [%] |
|---|---|---|---|---|
| | | $T_{max}$ [$K$] | | |
| | C01-E01 | 862.83 | 825.70 | -4.30 |
| | C01-E02 | 586.39 | 568.79 | -3.00 |
| | C01-E03 | 409.27 | 402.67 | -1.61 |
| Case 01 | C01-E04 | 1083.90 | 1082.29 | -0.15 |
| | C01-E05 | 886.41 | 862.78 | -2.67 |
| | C01-E06 | 586.37 | 568.79 | -3.00 |
| | C01-E07 | 456.39 | 447.07 | -2.04 |
| Case 02 | C02-E01 | 1382.77 | - | - |
| | C03-E01 | 1190.07 | 1145.63 | -3.73 |
| | C03-E02 | 708.78 | 700.34 | -1.19 |
| | C03-E03 | 507.18 | 499.98 | -1.42 |
| Case 03 | C03-E04 | 423.97 | 418.77 | -1.23 |
| | C03-E05 | 377.01 | 373.71 | -0.87 |
| | C03-E06 | 358.95 | 356.57 | -0.66 |
| | C03-E07 | 354.01 | 351.93 | -0.59 |
| | C04-E01 | 804.01 | 803.56 | -0.06 |
| Case 04 | C04-E02 | 943.02 | 943.99 | 0.10 |
| | C04-E03 | 948.77 | 945.42 | -0.35 |

Source: Own author.

Comparing the two performance indices, the maximum relative difference in the module was only 4.30% for C01-E01. However, the smallest relative difference was found in configuration C04-E01 with a value of 0.06%. Furthermore, the highest maximum temperature reached among all cases was in Case 02 in configuration C02-E01, with a value of 1382.77$K$. The lowest maximum temperature of 351.93$K$ was found in C03-E07 when using $CV$.

Figures 27-30 illustrate the temperature field generated on the plates with the welding process for all case studies. These figures show the results of best-performing configurations of $MAPE_m$.

Figure 27 – Temperature field - Case 01 - R01 - $\Delta t = 1.0s$.

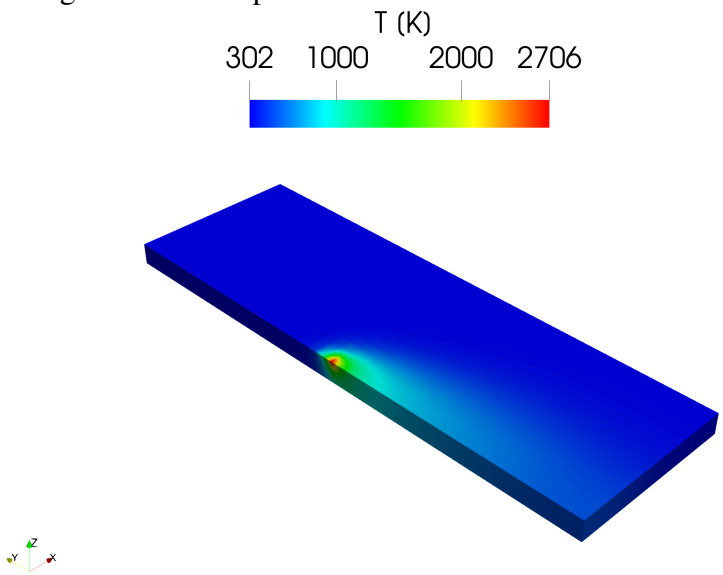


Source: Own author.

Figure 28 – Temperature field - Case 02 - R02 - $\Delta t = 1.0s$.

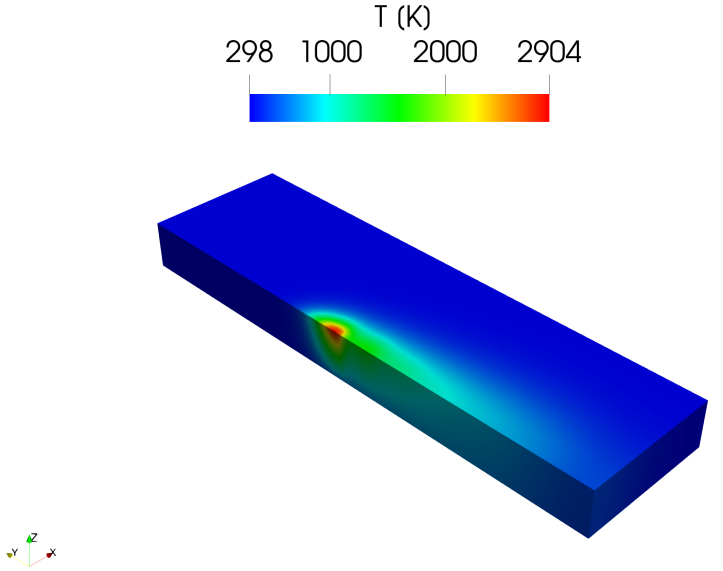


Source: Own author.

Figure 29 – Temperature field - Case 03 - R02 - $\Delta t = 1.0s$.

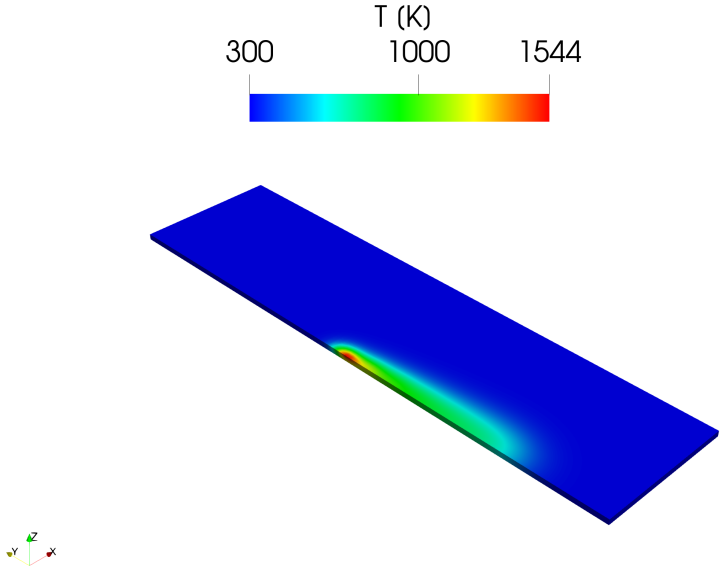


Source: Own author.

Figure 30 – Temperature field - Case 04 - R03 - $\Delta t = 1.0s$.

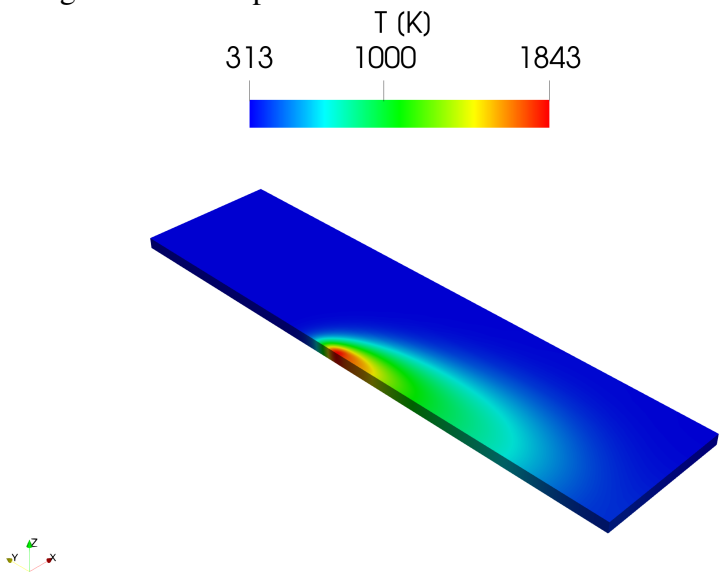


Source: Own author.

For Case 01, the time that the torch reaches the center of the plate is greater due to its welding velocity being the lowest among all cases. For all cases shown in Figures 27-30, maximum temperatures were generated around $2706K$, $2904K$, $1554K$ and $1843K$, respectively. The minimum temperature values correctly represent the ambient and initial temperatures of each case.

Table 10 shows the values of CPU times, illustrating the computational cost generated in simulations for all cases.

Table 10 – Computational cost in cases under study.

| Case | Mesh | $\Delta t = 0.25s$ $t_{CPU}$ $[s]$ | $\Delta t = 0.50s$ $t_{CPU}$ $[s]$ | $\Delta t = 1.0s$ $t_{CPU}$ $[s]$ | Total time $[h]$ |
|---|---|---|---|---|---|
| Case 01 | R01 | 566.55 | 287.71 | 151.79 | 7.70 |
| | R02 | 3143.64 | 1606.69 | 822.56 | |
| | R03 | 11865.89 | 6117.63 | 3158.04 | |
| Case 02 | R01 | 23.33 | 12.15 | 6.71 | 1.18 |
| | R02 | 647.20 | 332.93 | 189.00 | |
| | R03 | 1719.27 | 867.40 | 446.41 | |
| Case 03 | R01 | 569.41 | 291.10 | 151.62 | 8.85 |
| | R02 | 4475.72 | 2319.31 | 1164.49 | |
| | R03 | 12937.53 | 6635.68 | 3314.90 | |
| Case 04 | R01 | 1492.52 | 753.38 | 490.28 | 8.60 |
| | R02 | 3587.38 | 1848.88 | 948.95 | |
| | R03 | 12624.34 | 6096.41 | 3133.35 | |

Source: Own author.

For Case 03, there was the highest $t_{CPU}$, with approximately $8.85h$. This time is due because this case has more elements than the other cases. However, the smallest $t_{CPU}$ was found for Case 02, with $1.18h$. Table 10 illustrates the increase in $t_{CPU}$ with spatial and temporal refinement. This behavior occurs because it increases the number of calculations that the computer has to perform.

Finally, the thermal cycles found in prediction cases (Table 8) using the configurations that had the best performance with $MAPE_m$ are illustrated in Figures 31-34.

Figure 31 – Numerical predictions obtained - Case 01 - R01 - $\Delta t = 1.0s$.

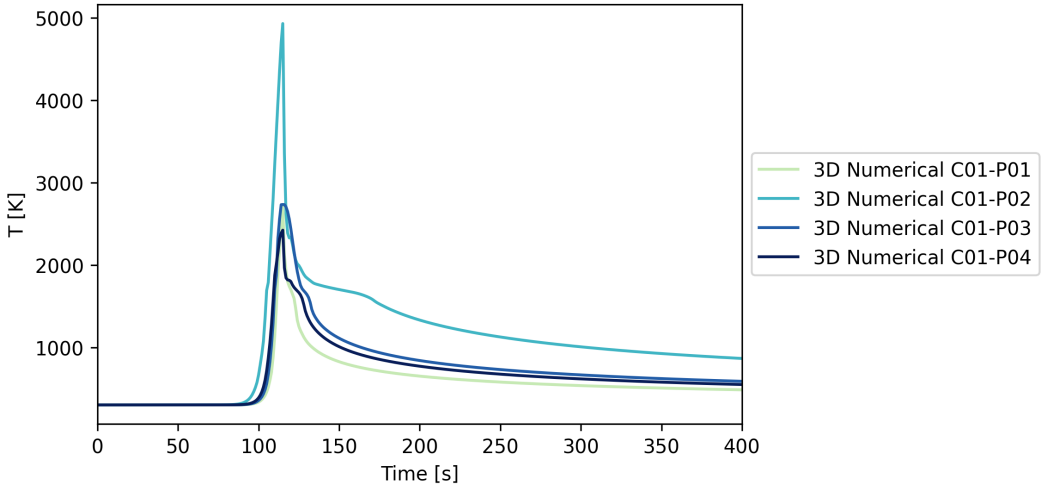


Source: Own author.

Figure 32 – Numerical predictions obtained - Case 02 - R02- $\Delta t = 1.0s$.

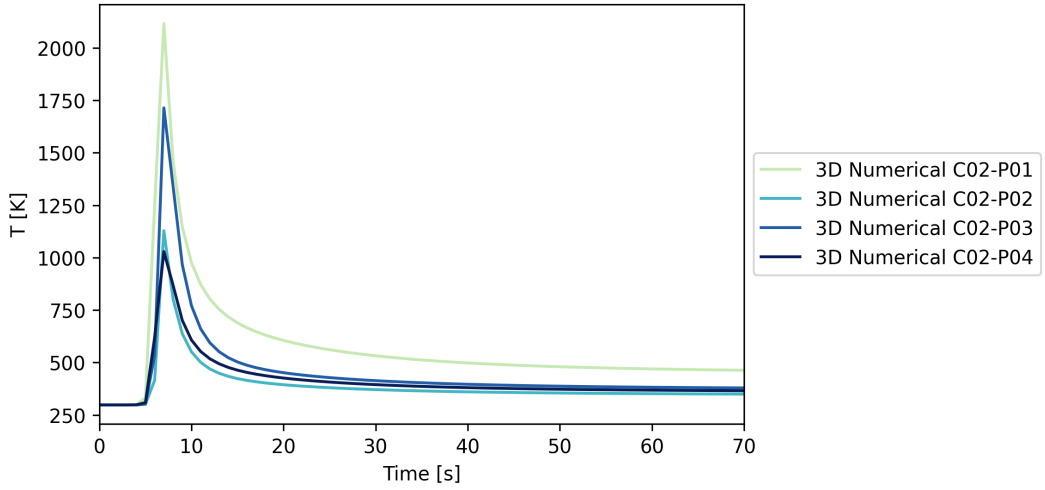


Source: Own author.

Figure 33 – Numerical predictions obtained - Case 03 - R02 - $\Delta t = 1.0s$.

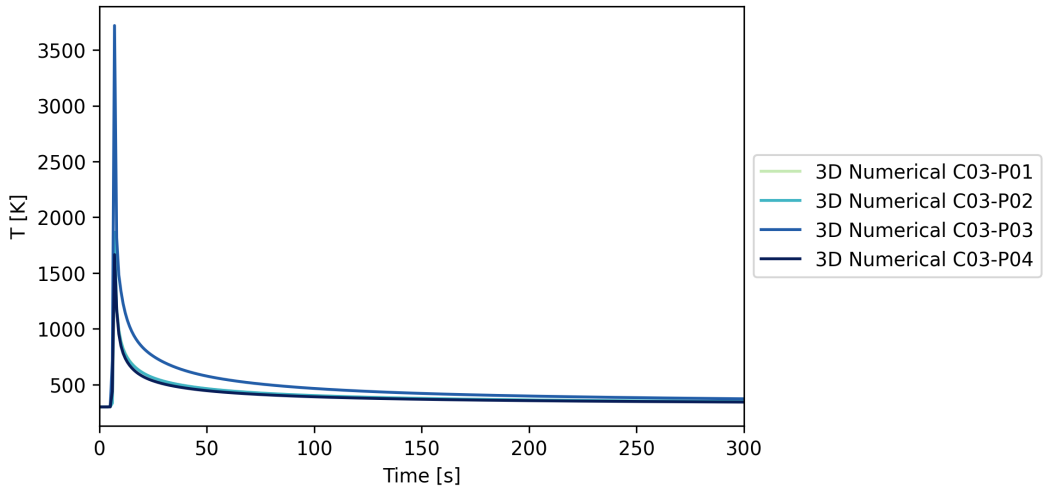


Source: Own author.

Figure 34 – Numerical predictions obtained - Case 04 - R03 - $\Delta t = 1.0s$.

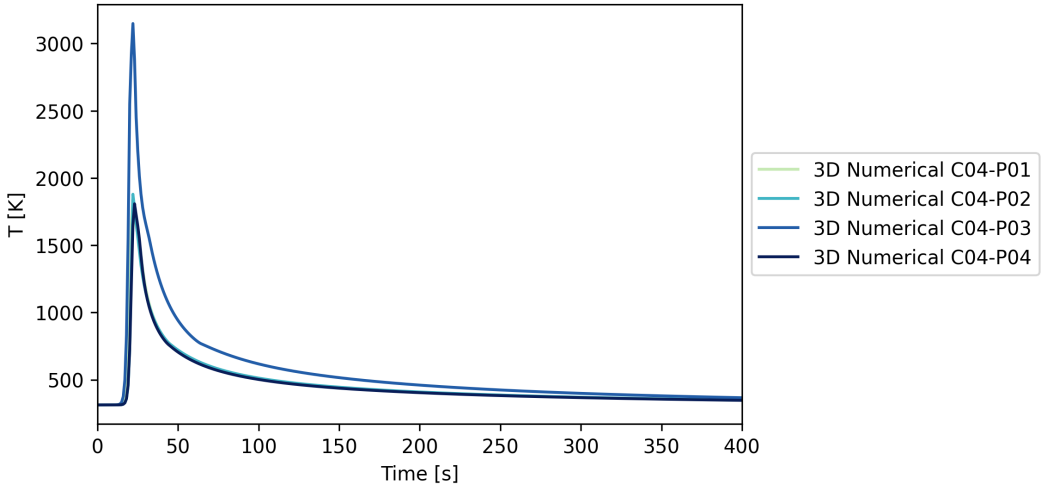


Source: Own author.

The shape of curves of predicted thermal cycles shows the similarity of behavior of temperatures validated in experimental cases. The maximum temperatures of these thermal cycles are shown in Table 11. The reference temperature is the first $T_{max}$ of each case, as it is the configuration that maintained the welding parameters of the respective experimental case.

Table 11 – Maximum temperatures in numerical predictions.

| Case | Label | $T_{max}$ $[K]$ | Relative difference $[\%]$ |
|---|---|---|---|
| Case 01 | C01-P01 | 2705.73 | Ref. |
| | C01-P02 | 4930.96 | 82.24 |
| | C01-P03 | 2734.88 | 1.08 |
| | C01-P04 | 2423.50 | -10.43 |
| Case 02 | C02-P01 | 2115.93 | Ref. |
| | C02-P02 | 1128.56 | -46.66 |
| | C02-P03 | 1714.10 | -18.99 |
| | C02-P04 | 1029.13 | -51.36 |
| Case 03 | C03-P01 | 1544.27 | Ref. |
| | C03-P02 | 1866.06 | 20.84 |
| | C03-P03 | 3719.18 | 140.84 |
| | C03-P04 | 1665.58 | 7.85 |
| Case 04 | C04-P01 | 1838.33 | Ref. |
| | C04-P02 | 1879.28 | 2.23 |
| | C04-P03 | 3148.26 | 71.26 |
| | C04-P04 | 1808.34 | -1.63 |

Source: Own author.

Among all cases, the highest predicted temperature value was $4930.96K$, which uses the welding parameters of Case 02 in configurations of Case 01, which has the lowest welding velocity. The lowest value was found for Case 02 using the welding parameters of Case 03, with

a maximum temperature of 1029.13$K$. Case 03 had the highest mean relative absolute difference among the other modifications, with a value of 56.51% resulting in a significantly greater change when changing settings. Case 04, had the lowest mean in relative absolute difference, with 25.04%. The extreme temperatures that appeared in some configurations aren't advised in a real TIG welding process as they exceed the melting point of the tungsten electrode which is 3683$K$ and cause problems in the final workpiece, in the electrode, and in the equipment used or directly the welder (MALLICK, 2010; MARQUES *et al.*, 2011).

Table 12 shows the computational costs in simulations performed to predict the thermal cycles in predicted cases. As there are 4 options in each predicted case, the mean $t_{CPU}$ was calculated. Case 04 resulted in the highest $(t_{CPU})_m$ of 3093.26$s$ with a total CPU time of 3.44$h$, among the other cases. This occurred because this case had a greater number of elements.

Table 12 – Computational cost of numerical prediction cases.

| Predicted cases | $(t_{CPU})_m$ [$s$] | Total time [$h$] |
|---|---|---|
| Case 01 | 151.02 | 0.17 |
| Case 02 | 171.25 | 0.19 |
| Case 03 | 1146.30 | 1.27 |
| Case 04 | 3093.26 | 3.44 |

Source: Own author.

## 3.4 Conclusions

In the present study, a numerical analysis of TIG welding process on rectangular plates using austenitic stainless steels (316L, 316 and 304) was performed using a thermal simulator based on EbFVM and compared with experimental results of thermal cycles generated in the process. The influence of spatial and temporal refinement was investigated. The performance of simulations was compared using the MAPE and CV metrics and their computational cost. In addition, predictions were obtained by modifying some welding parameters, seeking to understand the thermal behavior in these new situations. Based on the general numerical analysis performed, the following observations were made:

- The modeling of the welding process using the double ellipsoidal source proved to be a good option to represent the TIG process, as it generated a compatible behavior when compared to the experimental one;
- The MAPE performance comparison metric showed good results, with relatively low

values in four cases, between 2.92% and 7.67%. Case 01 had lower MAPE values, on the mean, and Case 04 had the highest values. Regarding the CV, values between 0.162 and 1.04 were found. Case 04 had a more homogeneous behavior and Case 03 the least homogeneous when compared to each other;

- The mesh refinement generated a decrease in mean MAPE values in most cases. In addition, it caused greater homogeneity, through the CV, in most of the configurations of case studies, mainly in Case 01;
- The temporal refinement in each time step generated an increase in mean values of MAPE, in all cases. Furthermore, this refinement generated greater homogeneity in most configurations of cases under study;
- The numerical-experimental comparison showed sufficient proximity to illustrate the efficiency of the procedure performed;
- The absolute relative difference between the maximum temperatures of numerically calculated thermal cycles didn't exceed 4.30%, showing a certain proximity between the best result with $MAPE_m$ and with $CV$;
- The heat map generated in the welding process illustrated the behavior and fidelity of the heat source when compared with the experimental results;
- The prediction of new configurations for the cases under study showed a possible behavior of temperature distribution respecting the physical logic found in experimental processes;
- The simulated cases confirmed that with the refinement of both the mesh and the time intervals of each step, the computational cost will be higher. For the cases under study, combining experiments and predictions, totaled 31.40$h$ of CPU time.

# 4 THERMAL ANALYSIS OF TIG WELDING WITH AUSTENITIC STAINLESS STEELS USING DEEP LEARNING

## 4.1 Review

This work sought to present a faster way to thermally analyze the autogenous TIG welding process on plates using austenitic stainless steels (316L and 304) through deep learning. Neural network structures were used with deep learning algorithms in Python to predict the thermal cycles of two experimental cases from the literature. In order to enhance the breadth of available options, the database was enriched through the incorporation of additional numerical simulations. These simulations encompassed the cases previously validated in the preceding chapter, with deliberate adjustments made to the welding parameters. This approach ensured a more comprehensive coverage of potential scenarios within the database. The construction of the deep learning network was approached in two ways: Firstly, by dividing it into five networks, with each network dedicated to one of the five fundamental points that characterize the thermal cycle. Secondly, by using a single network to capture the entire temperature distribution. The data were divided in the proportion of 80-20% between training (estimation with validation) and testing. To determine the optimal hyperparameters for training the network, a cross-validation methodology was employed. This approach ensured that the errors on the test data remained below 5%, indicating a high level of accuracy and reliability in the results. This applied methodology proved to be efficient when quantitatively and qualitatively compared with experimental and numerical curves. The computational cost to predict the temperatures after construction and training the networks is minimal. Thus, this tool becomes a great strategy for this type of application.

## 4.2 Materials and methods

### *4.2.1 Data preparation and collection*

Initially, the main variables that directly influence the thermal cycle of the welding process were stipulated. Among the existing categories of parameters, eleven variables were defined that best summarize and represent the boundary conditions used in the simulation of TIG welding on plates. As seen in the previous chapter, the analyzed plates were divided symmetrically in relation to the bead weld. Figure 35 illustrates this division and the variables considered in the problem. Therefore, one of the variables represents the symmetrical width of

the plate ($w_p$). In addition to this, there is the thickness of the plate ($t_p$), the length of the weld bead ($l_{wb}$), the position in $y$ at which the welding process begins ($s_w$), the ambient temperature ($T_\infty$), the type of material used ($M$) maintaining the thermal properties ($\rho$, $c_p$ and $k$ ) respectively, the mean global heat transfer coefficient ($h_m$) between the smallest and the largest values, the input heat in relation to welding velocity ($H_w = \frac{S}{v_w}$), and the relative positions on the plate relative to the starting point of process ($x_r$, $y_r$, $z_r$).

Figure 35 – Plate with the variables defined.

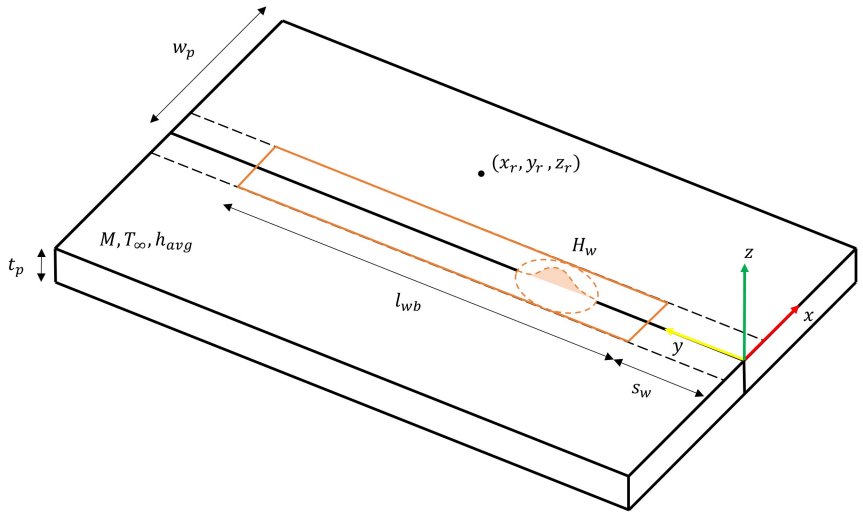


Source: Own author.

After defining the variables, two cases were chosen from the set of cases studied in the previous chapter. The selection was based on identifying the cases with greater homogeneity in their errors, determined by a lower coefficient of variation (CV) indicator. This information fed the database that was used to train the deep learning network. These data were obtained with simulations of Cases 01 (R03 - $\Delta t = 0.25s$) and 04 (R01 - $\Delta t = 0.25s$), modifying the variables that address the welding parameters and positions on the plate. It's worth pointing out for Case 04 was chosen as the second best configuration as it would considerably reduce the computational cost and not affect the efficiency of analysis. This CV difference between the best configuration and the second best configuration, in this case, was 1.85%. The input heat values used in simulations that fed the database were slightly different from the original

ones applied in chosen cases. This strategy was adopted to cover more options in the analysis. The same reasoning was applied to the relative positions ($x_r$, $y_r$, $z_r$) of plate. The heat source parameters were maintained according to the total heat input $S$ of each case. The simulation time of 400$s$ and the mesh configurations also followed the same for selected cases. The material type was defined as $M = 0$ for 304 steel and $M = 1$ for 316L steel. In addition, an extra value of $h_m = 40 W m^{-2} K^{-1}$ found in literature was added to have an extra option in analysis. Therefore, 20736 combinations were simulated in total (size of dataset). Table 13 illustrates all variables and their defined values.

Table 13 – Description and values of defined variables.

| Category | No. | Variable | Label | Unit | Case 01 | Case 04 | Simulated options |
|---|---|---|---|---|---|---|---|
| Geometry | 1 | Symmetrical plate width | $w_p$ | $[mm]$ | 80 | 37.5 | 37.5 and 80 |
| | 2 | Plate thickness | $t_p$ | $[mm]$ | 10 | 3 | 3 and 10 |
| Initial condition | 3 | Weld bead length | $l_{wb}$ | $[mm]$ | 230 | 110 | 110 and 230 |
| | 4 | Welding start position | $s_w$ | $[mm]$ | 10 | 20 | 10 and 20 |
| | 5 | Ambient temperature | $T_\infty$ | $[K]$ | 302 | 313 | 302 and 313 |
| Properties | 6 | Type of material | $M$ | - | 1 | 0 | 0 and 1 |
| | 7 | Mean global heat transfer coefficient | $h_m$ | $[W m^{-2} K^{-1}]$ | 10 | 172.85 | 10, 40 and 172.85 |
| Welding parameters | 8 | Heat input in welding | $H_w$ | $[J mm^{-1}]$ | 1020 | 590.16 | 365, 480, 1095 and 1440 |
| Plate positions | 9 | Relative position x | $x_r$ | $[\%]$ | 0, 10, 12.5, 25, 43.75 and 62.5 | 20 and 25.33 | 0, 25 and 50 |
| | 10 | Relative position y | $y_r$ | $[\%]$ | 36.96 | 25, 50 and 75 | 25, 50 and 75 |
| | 11 | Relative position z | $z_r$ | $[\%]$ | 0 and 100 | 100 | 0, 50 and 100 |

Source: Own author.

### *4.2.2 Deep learning simulation*

#### *4.2.2.1 Model construction*

The deep learning model adopted two types of construction. Type 01 considers five specific points that illustrate the behavior of the thermal cycle in Figure 36. The first two points refer to time and temperature where the first appearance of a temperature value 5% higher than the initial temperature occurs. The third and fourth points refer to time and temperature where the highest temperature value occurs in a cycle. The last point refers to the temperature value

at the end of the simulation ($t = 400s$). Type 02 considers all thermal cycle temperature values during the $400s$ simulation with a single network, with a step-time of $1.0s$. Table 14 summarizes these types, detailing the number of networks and neurons in input and output layers.

Figure 36 – Specific points in the thermal cycle.

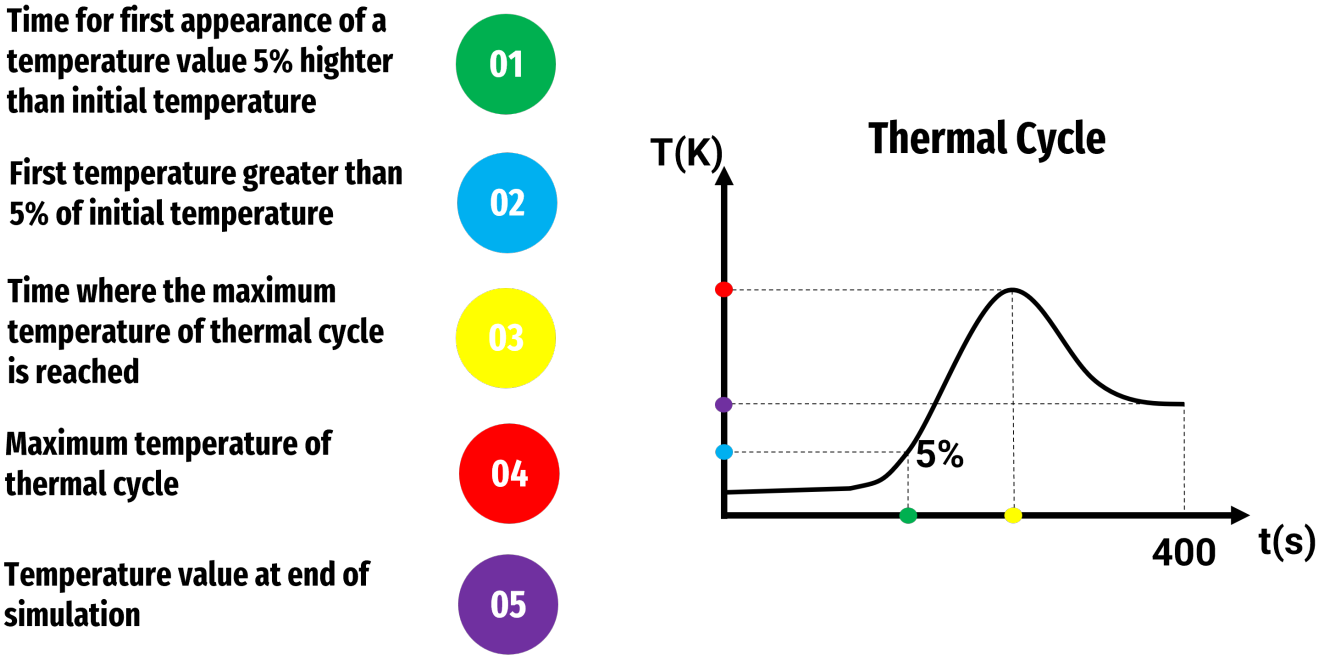


Source: Own author.

Table 14 – Build types for the deep learning model.

| Type | Qty. network | Qty. neuron | | Description |
|---|---|---|---|---|
| | | Input layer | Output layer | |
| Type 01 | 5 | 11 | 1 | A network to predict the temperature in specific points. |
| Type 02 | 1 | 11 | 401 | A network to predict the complete thermal cycle. |

Source: Own author.

To find the hidden layers, the possible number of layers and neurons was stipulated, using Geometric Mean (GM), Arithmetic Mean (AM), and Weighted Mean (PM). The calculation of these layers followed the pattern illustrated in Figure 37.

Figure 37 – Example of how the means used in study are calculated.

***To 2 hidden layers***:

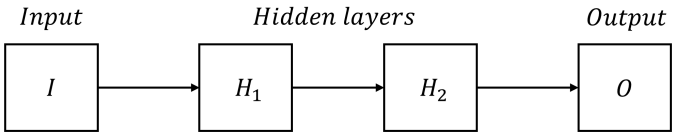


***GM – Geometric Mean***:

$$H_1 = \sqrt{IH_2}$$

$$H_2 = \sqrt{H_1 O}$$

***AM – Arithmetic Mean***:

$$H_1 = \frac{I + H_2}{2}$$

$$H_2 = \frac{H_1 + O}{2}$$

***PM (A: B) – Weighted arithmetic mean***:

$$H_1 = \frac{(I\ x\ A) + (H_2\ x\ B)}{(A + B)}$$

$$H_2 = \frac{(H_1\ x\ A) + (O\ x\ B)}{(A + B)}$$

Source: Own author.

Therefore, the number of neurons was calculated, rounding the values found in geometric, arithmetic and weighted mean with the weights 2:1, 3:2, 3:1, 4:1, 4:3 for Type 01, varying the number of hidden layers from 2 to 7. For Type 02, , the same logic was used, but the weights were inverted because the number of neurons in output is greater than the input. The results of these calculations are illustrated in Tables 15, 16 and 17:

Table 15 – Distribution of neurons for Type 01.

| Mean | Qty. hidden layers | | | | | |
|---|---|---|---|---|---|---|
| | 2 | 3 | 4 | 5 | 6 | 7 |
| GM | [5,2] | [6,3,2] | [7,4,3,2] | [7,5,3,2,1] | [8,6,4,3,2,1] | [8,6,4,3,2,2,1] |
| AM | [8,4] | [8,6,3] | [9,7,5,3] | [9,8,6,4,3] | [10,8,7,5,4,2] | [10,8,7,6,5,3,2] |
| PM (2:1) | [10,7] | [10,9,6] | [11,10,9,6] | [11,11,10,9,6] | [11,11,10,10,9,6] | [11,11,11,10,10,9,6] |
| PM (3:2) | [9,6] | [10,8,5] | [10,9,7,5] | [11,10,9,7,5] | [11,10,10,8,7,5] | [11,10,10,9,8,7,4] |
| PM (3:1) | [10,8] | [11,10,8] | [11,11,10,8] | [11,11,11,10,8] | [11,11,11,11,10,8] | [11,11,11,11,11,10,8] |
| PM (4:1) | [11,9] | [11,10,9] | [11,11,10,9] | [11,11,11,10,9] | [11,11,11,11,10,9] | [11,11,11,11,11,10,9] |
| PM (4:3) | [9,5] | [9,7,5] | [10,9,7,4] | [10,9,8,6,4] | [10,10,9,8,6,4] | [11,10,9,9,7,6,4] |

Source: Own author.

Table 16 – Distribution of neurons for Type 02 - Qty. hidden layers 2-4.

| Mean | Qty. hidden layers | | |
|---|---|---|---|
| | 2 | 3 | 4 |
| GM | [36,121] | [27,66,163] | [23,46,95,195] |
| AM | [141,271] | [108,206,303] | [89,167,245,323] |
| PM (1:2) | [234,345] | [219,323,375] | [212,313,363,388] |
| PM (2:3) | [196, 319] | [173, 281, 353] | [161,261,327,371] |
| PM (1:3) | [281,371] | [274,362,391] | [272,359,388,398] |
| PM (1:4) | [308,382] | [305,378,396] | [304,377,395,400] |
| PM (3:4) | [180,306] | [154,261,341] | [139,235,307,361] |

Source: Own author.

Table 17 – Distribution of neurons for Type 02 - Qty. hidden layers 5-7.

| Mean | Qty. hidden layers | | |
|---|---|---|---|
| | 5 | 6 | 7 |
| GM | [20,36,66,121,220] | [18,31,51,86,144,240] | [17,27,42,66,104,163,256] |
| AM | [76,141,206,271,336] | [67,122,178,234,290,345] | [60,108,157,206,255,303,352] |
| PM (1:2) | [209,308,358,382,395] | [208,306,355,380,392,398] | [207,305,354,378,390,396,399] |
| PM (2:3) | [154,249,312,354,382] | [149,241,303,343,371,389] | [146,236,297,337,363,381,393] |
| PM (1:3) | [271,358,387,397,400] | [271,358,387,396,400,401] | [271,358,387,396,399,401,401] |
| PM (1:4) | [304,377,395,400,401] | [304,377,395,400,401,401] | [304,377,395,399,401,401,401] |
| PM (3:4) | [130,219,285,335,373] | [124,208,271,319,354,381] | [119,201,262,307,342,367,387] |

Source: Own author.

#### *4.2.2.2 Training and testing*

With the data organized for each type of model, the group was divided into two parts: one for training and another for testing, in a ratio of 80-20%, in that order. Within the training, the Cross-validation technique was used to evaluate the best option for the hidden layers. All layers defined in Tables 15-17 were applied, using the optimizer Root Mean Squared Propagation (RMSPROP), the Mean Squared Logarithmic Error (MSLE) loss function, the number of epochs equal to 50, the batch size equal to 16, the Mean Squared Error (MSE) metric and a cross-validation subdivision equal to $k = 5$. It was chosen to fix the other hyperparameters due to the high computational cost. This process was carried out in 6 different networks of two types of models previously defined. With the distribution of neurons and layers established, further comparisons were performed to understand the behavior and choose the best final combination for each network. A new comparison was made by varying the optimizer (rmsprop, Adam, and Stochastic gradient descent (SGD)), loss function (MSLE, MAPE, MAE), and fixing the other parameters. The RELU activation function and the standard learning rate and momentum hyperparameters were maintained in all analyzed comparisons. All these parameters were defined

according to the literature found on the application of deep learning in engineering problems. Finally, the separate test data (20.0%) were applied to models with the best combinations found in analyzed comparisons.

#### *4.2.2.3 Predictions*

After the deep learning networks were trained and tested, it was possible to apply the original input values of Cases 01 and 04 in final Deep Learning (DL) models found to predict the points in two types of networks, present in Table 13. Therefore, the comparison between simulated values using EbFVM and those predicted with Deep Learning can be performed, verifying the performance of the applied methodology.

## 4.3 Results

Case 04, so-called in text until then, will be called Case 02 to simplify the text, from that point on. In the first comparison, the best combinations of hidden layers for both types were indicated. Figure 38 shows the results obtained with the Grid Search for the five points of Type 01, where it is possible to visualize the configurations with the smallest errors in each point, illustrated by a normalized score.

Figure 38 – Score x Settings - Type 01.

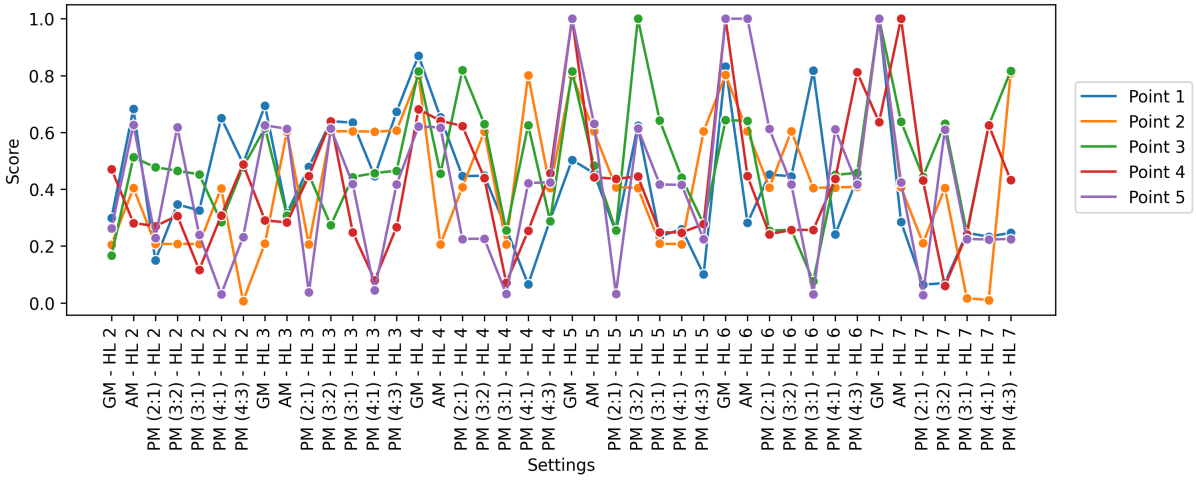


Source: Own author.

In addition, these results were organized by categorizing by the number of hidden layers and the chosen mean, to understand the influence of each of these variables on the error values, which can be seen in boxplots of Figure 39.

Figure 39 – Boxplot analysis based on a hidden layer and mean settings - Type 01.

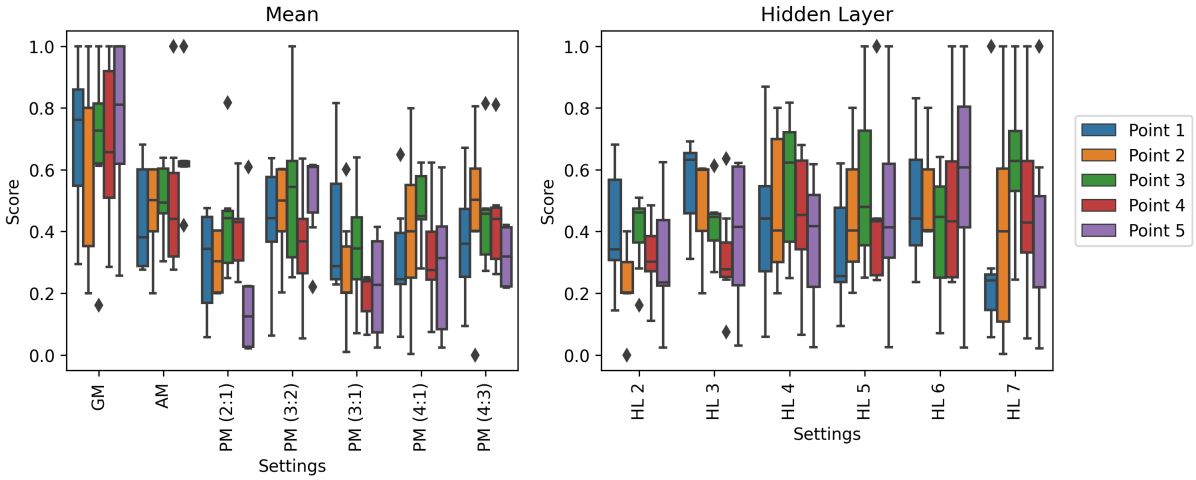


Source: Own author.

The GM presented the worst performance in analyzed points, while the PM presented the best mean values, with the lowest scores. Furthermore, regarding the number of hidden layers, the option with 2 layers, visually, presented lower mean scores in general.

The same analysis was performed for Type 02, resulting in Figure 40 that illustrates the values obtained in all the configurations tested in Grid Search.

Figure 40 – Score x Settings - Type 02.

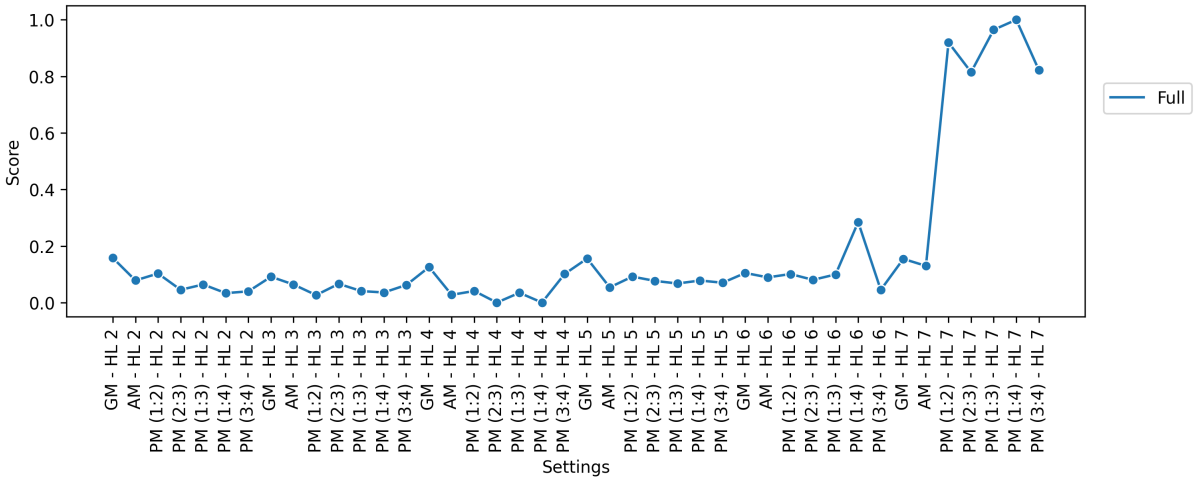


Source: Own author.

From Figure 40 it was possible to visualize a worse performance, higher scores, for the weighted mean group (PM) with 7 hidden layers. However, in the same mean type with 4 layers, there was a better performance in general. Figure 41 confirms this behavior showing the boxplot separated by mean type and by the number of hidden layers.

Figure 41 – Boxplot analysis based on hidden layer and of mean type - Type 02.

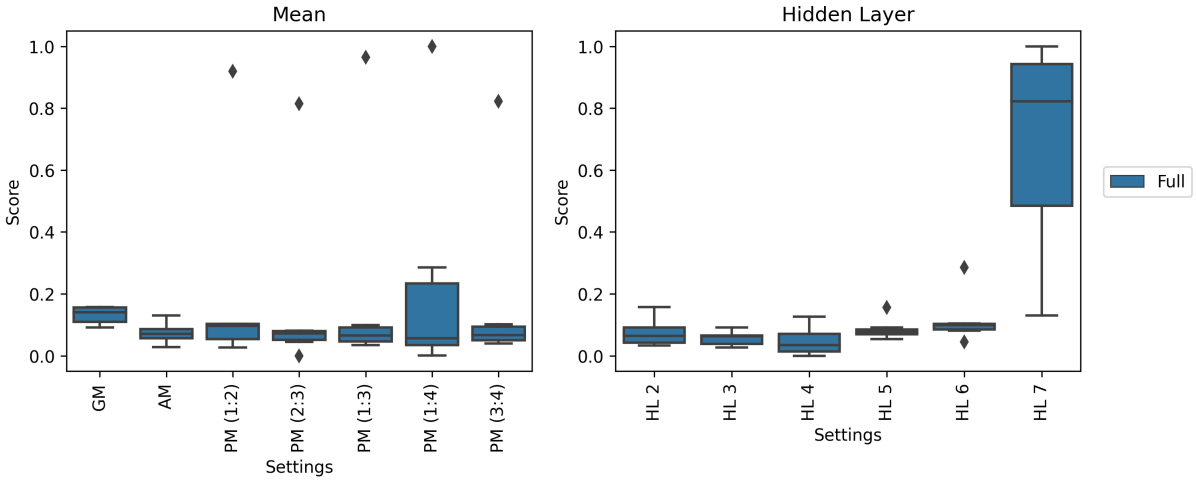


Source: Own author.

From the best options found in first comparison, the second comparison was performed, varying the optimizer and the loss function as defined in methodology. Similar to the previous procedure, the influence of these parameters can be seen through Figures 42 and 43 for Type 01 and Type 02, respectively.

Figure 42 – Boxplot analysis based on optimizer and of loss function - Type 01.

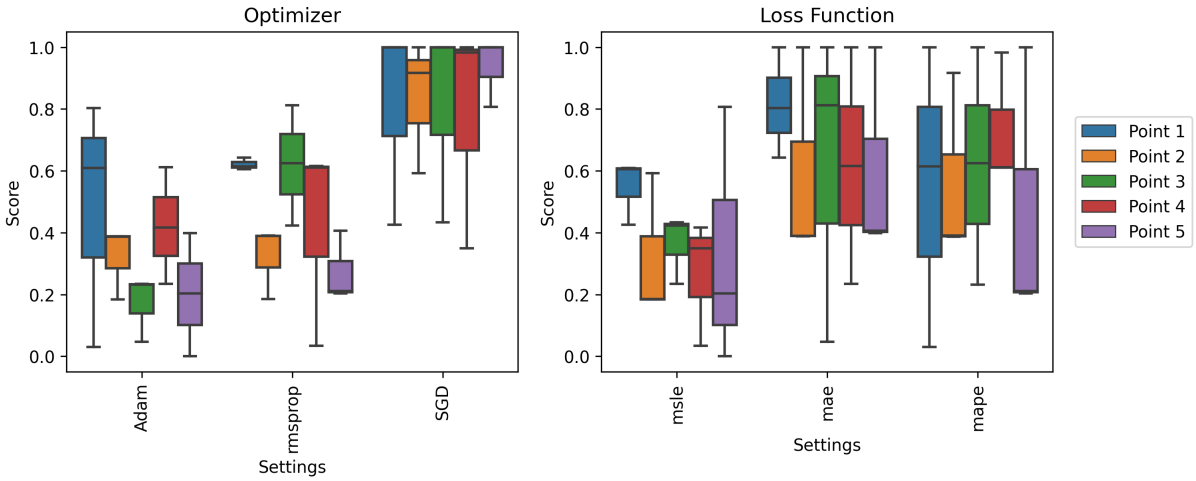


Source: Own author.

Figure 43 – Boxplot analysis based on optimizer and of loss function - Type 02.

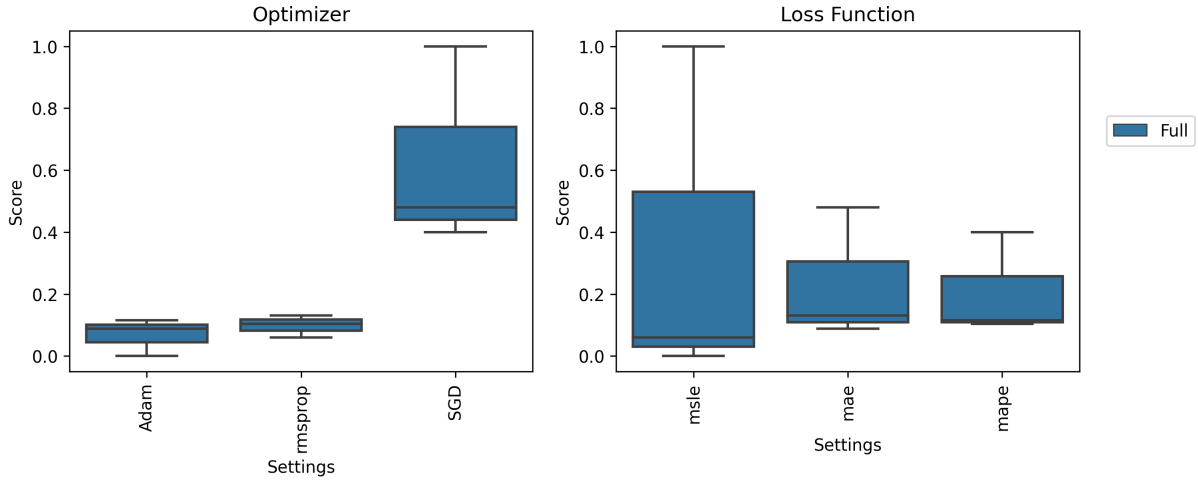


Source: Own author.

Based on the methodology adopted to choose the best configuration among those defined and analyzing the comparisons made, the ones that had the best performance were found and presented in Table 19.

Table 18 – Combinations with the best performances.

| Type | Point | Setting | Distribution | Optimizer | Loss Function |
|---|---|---|---|---|---|
| | Point 1 | PM (2:1) - HL 7 | [11,11,11,10,10,9,6] | Adam | MAPE |
| | Point 2 | PM (4:3) - HL 2 | [9,5] | Adam | MSLE |
| Type 01 | Point 3 | PM (3:1) - HL 6 | [11,11,11,11,10,8] | Adam | MAE |
| | Point 4 | PM (3:2) - HL 7 | [11,10,10,9,8,7,4] | Rmsprop | MSLE |
| | Point 5 | PM (2:1) - HL 7 | [11,11,11,10,10,9,6] | Adam | MSLE |
| Type 02 | Full | PM (2:3) - HL 4 | [161,261,327,371] | Adam | MSLE |

Source: Own author.

From these configurations, the networks were trained with 80% of data separated for training, increasing the epoch number from 50 to 200, but keeping the other hyperpameters fixed. Among the 6 networks, the network used for point 4 of Type 01 was increased to 400, as it had better MAPE results than with 200. For this phase, loss curves were generated with all data, both training and of test, according to the loss function of each type in Table 19 These curves for the five Type 1 networks and for the Type 2 network are illustrated in Figures 44-49.

Figure 44 – Loss curves generated in training and testing deep learning networks - Point 01 - Type 01.

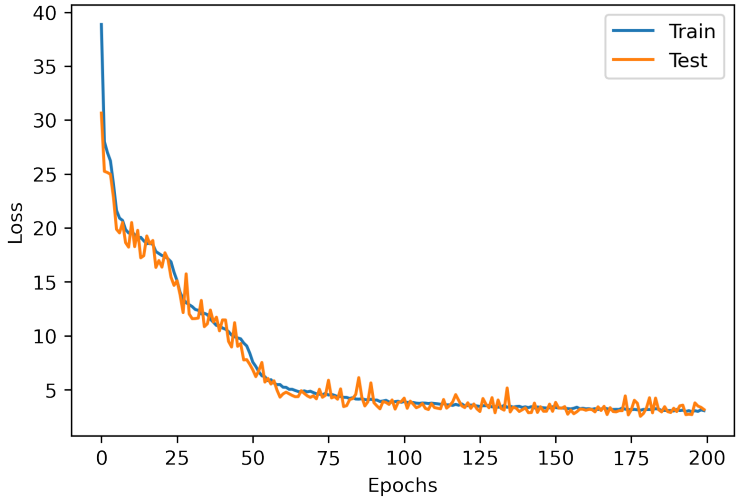


Source: Own author.

Figure 45 – Loss curves generated in training and testing deep learning networks - Point 02 - Type 01.

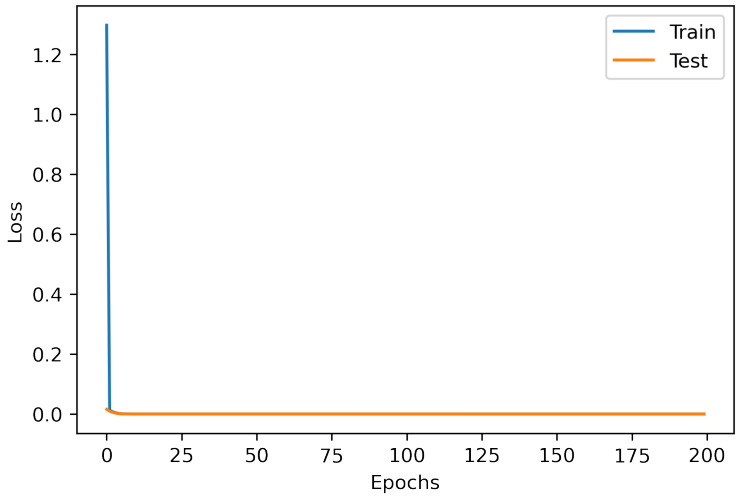


Source: Own author.

Figure 46 – Loss curves generated in training and testing deep learning networks - Point 03 - Type 01.

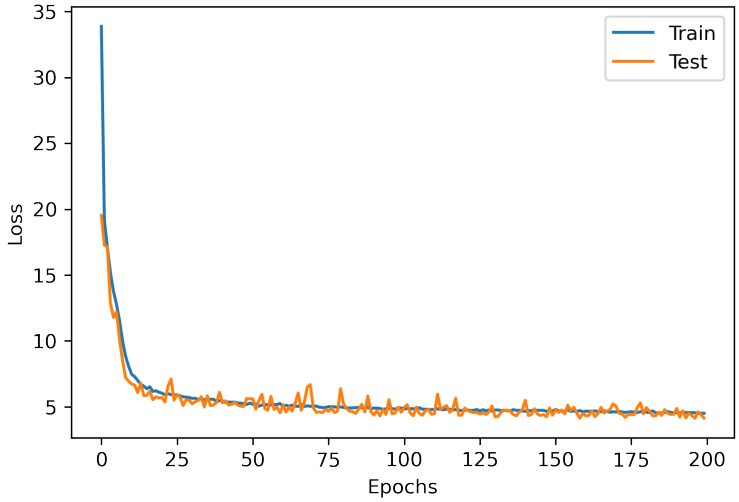


Source: Own author.

Figure 47 – Loss curves generated in training and testing deep learning networks - Point 04 - Type 01.

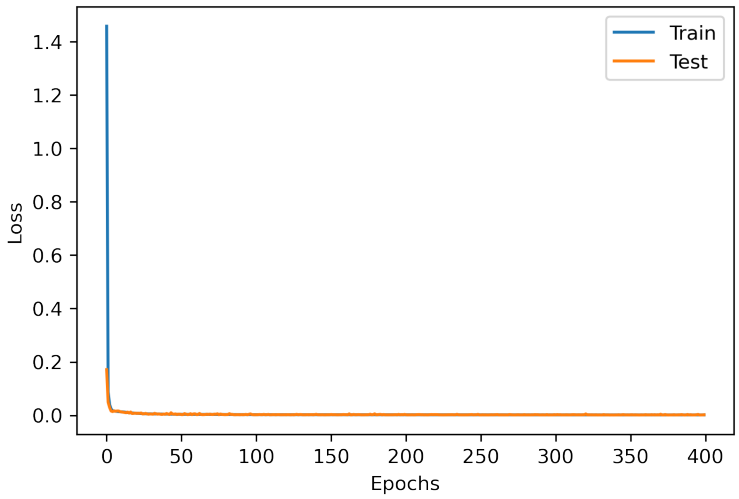


Source: Own author.

Figure 48 – Loss curves generated in training and testing deep learning networks - Point 05 - Type 01.

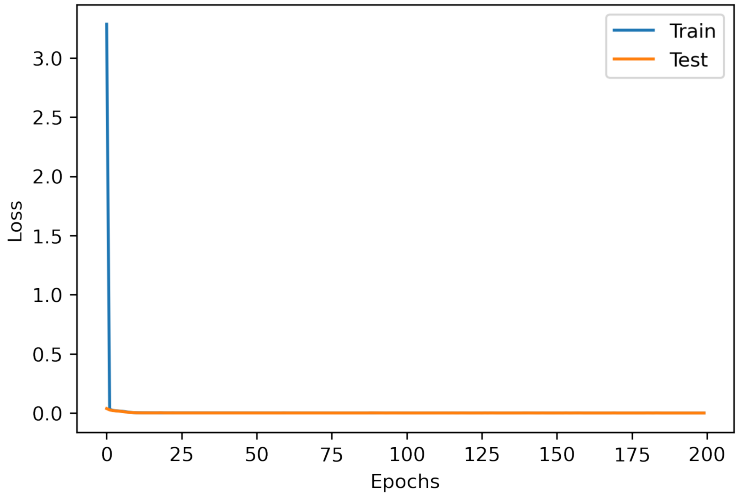


Source: Own author.

Figure 49 – Loss curves generated in training and testing deep learning networks - Full - Type 02.

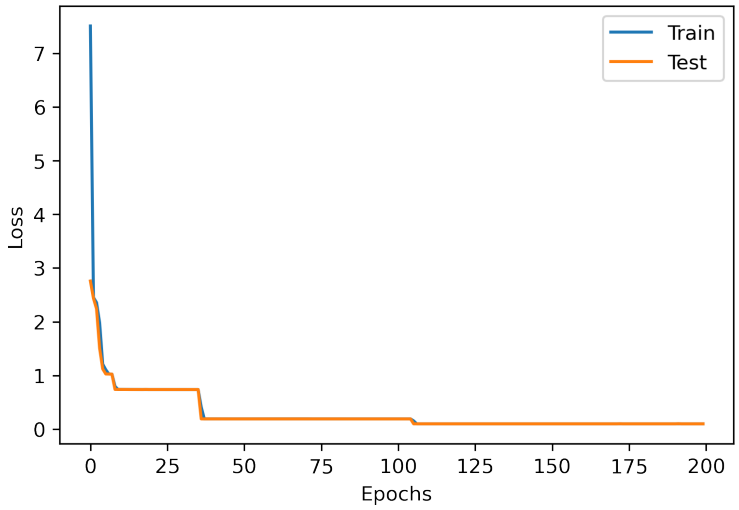


Source: Own author.

All curves showed a decrease in loss as the number of epochs was increased for both training and test data. Therefore, the MAPE index was calculated to verify the error generated by these networks. Table 19 shows these values in both types.

Table 19 – MAPE performance of training and test data.

| Type | Point | Epochs | Train [%] | Test [%] |
|---|---|---|---|---|
| | Point 1 | 200 | 3.186 | 3.157 |
| | Point 2 | 200 | 0.438 | 0.435 |
| Type 01 | Point 3 | 200 | 4.547 | 4.622 |
| | Point 4 | 400 | 3.639 | 3.562 |
| | Point 5 | 200 | 1.786 | 1.759 |
| Type 02 | Full | 200 | 1.073 | 1.073 |

Source: Own author.

It can be seen that the maximum MAPE error percentage was 4.622% in data from point 3 of Type 01 and the lowest in point 2, with 0.435%. With these networks found, it was possible to predict the thermal cycle for both types. Figures 50-53 show a comparison of values predicted by Deep Learning, with the results numerically simulated by EbFVM used in training and with the experimental results of selected cases.

Figure 50 – Type 01 Comparison - Deep Learning x 3D Numerical x Experimental - Case 01.

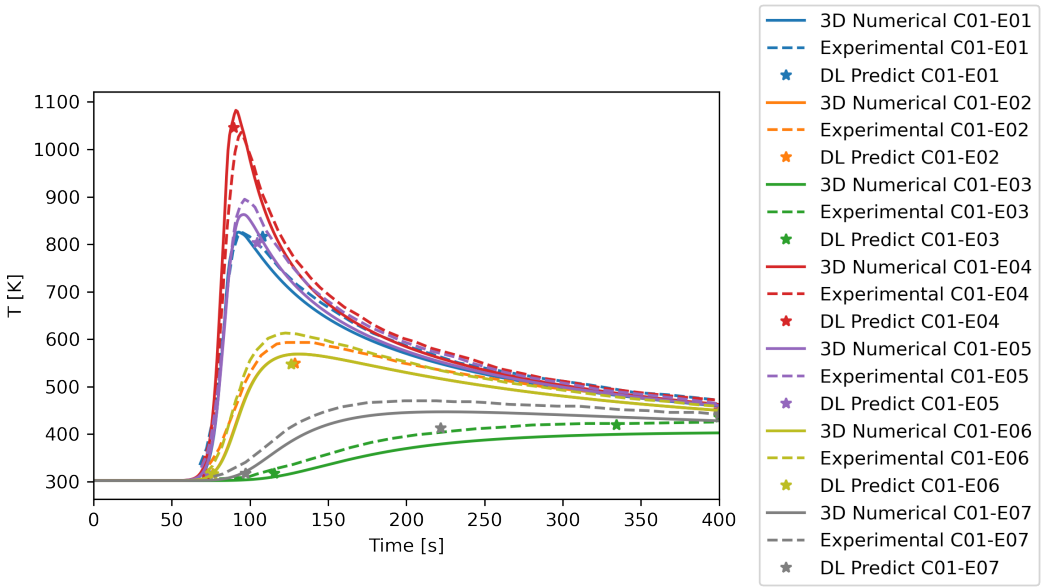


Source: Own author.

Figure 51 – Type 01 Comparison - Deep Learning x 3D Numerical x Experimental - Case 02.

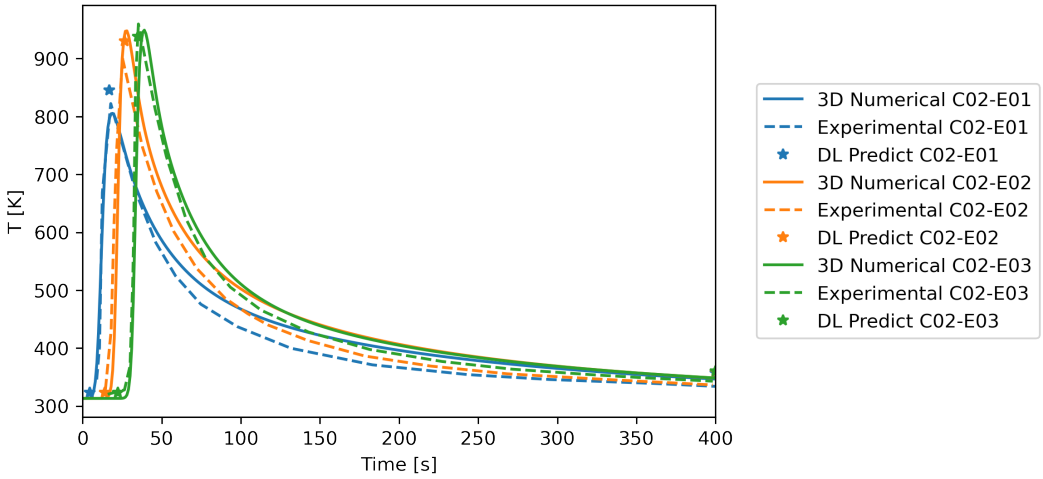


Source: Own author.

Figure 52 – Type 02 Comparison - Deep Learning x 3D Numerical x Experimental - Case 01.

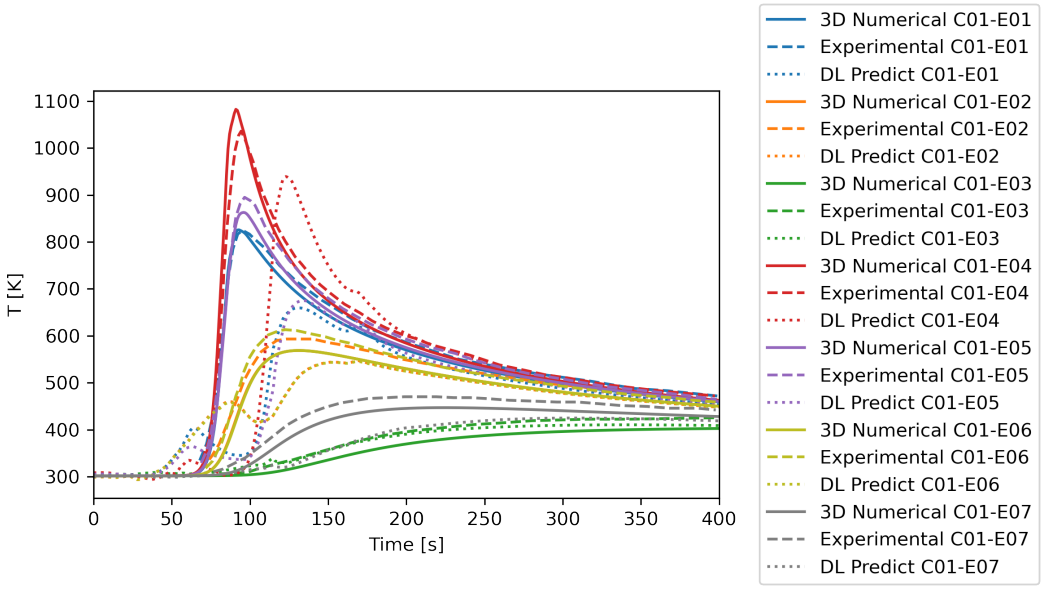


Source: Own author.

Figure 53 – Type 02 Comparison - Deep Learning x 3D Numerical x Experimental - Case 02.

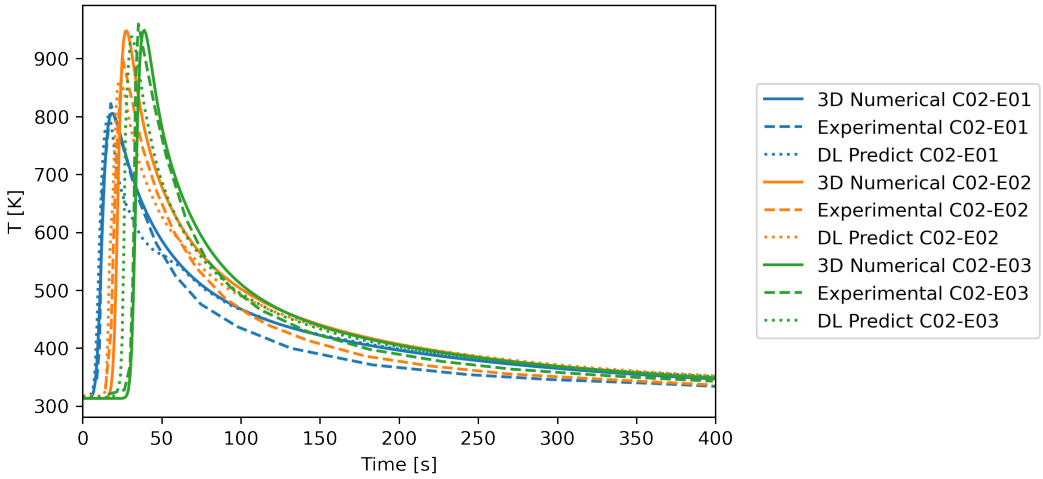


Source: Own author.

For both types, an extra treatment was performed to transform null temperature results into values calculated with the interpolation between two equidistant times. Visually, it is noted that the Type 01 results showed a close temperature distribution with the compared curves, representing the expected behavior well. Type 02, also had similar behaviors, but in Case 01, an extra smaller peak was presented at the beginning of the cycle. Table 20 it is possible to visualize the MAPE errors obtained by comparing these curves.

Table 20 – MAPE performance of proposed comparisons.

| Type/Case | | MAPE | | |
|---|---|---|---|---|
| | | Experimental [Ref.] x 3D Numerical [%] | 3D Numerical [Ref.] x DL Predict [%] | Experimental [Ref.] x DL Predict [%] |
| Type 01 | Case 01 | 4.48 | 3.96 | 18.72 |
| | Case 02 | 7.60 | 4.73 | 4.33 |
| Type 02 | Case 01 | 4.48 | 6.29 | 15.48 |
| | Case 02 | 7.60 | 3.07 | 13.66 |

Source: Own author.

Table 20 shows that the maximum MAPE for the 3D Numerical x DL Predict comparison was 4.73% for Type 01 and 6.29% for Type 2. These errors can be considered low since visually the curves were very close. However, in the Experimental x DL Predict comparison, it had a maximum MAPE of 18.72% for Type 01 and 15.48% for Type 02. Despite these errors, similar behaviors can also be noticed visually, mainly in Case 02.

## 4.4 Conclusions

In this study, a thermal analysis of the autogenous TIG welding process on rectangular plates using austenitic stainless steels (316L and 304) was performed using deep learning algorithms and compared the predicted thermal cycles with the experimental results and numerically simulated with EbFVM. The MAPE performance index was used to compare errors between curves. Two types of deep learning network construction architecture were developed and compared with each other. In addition, the influence of hyperparamters used in the construction of deep learning models was investigated. Based on the analysis carried out, the following observations were made:

- The choice of variables that characterize the autogenous TIG welding process applied to austenitic stainless steels proved to be efficient;
- Simulations of all planned combinations form a good dataset to feed deep learning networks;
- The two deep learning network construction frameworks gave different views on how to arrive at efficient prediction results;
- The methodology adopted through meantypes, number of hidden layers and variation of hyperparameters to choose the best ways to construct the network brought a good prediction of thermal behavior in this welding process;
- The training of networks generated errors of less than 5% in tests performed;
- Most networks construct had better results when using the Adam optimizer, loss function MSLE, weighted average, and number of hidden layers greater than or equal to 6;
- The loss curves confirmed that the amount of epoch number used was sufficient to generate good forecasts with low errors;
- The comparison between the thermal cycles of experimental cases, those numerically simulated with EbFVM, and deep learning predictions showed that visually the curves were very close. Furthermore, in a quantitative sense, errors lower than 6.3% were obtained when comparing DL Predict with the numerically simulated ones and lower than 18.8% when compared with the experimental cases;
- Finally, with this methodology used, there was a solution to predict thermal cycles with low computational cost when compared to numerical simulations.

# 5 CONCLUSIONS AND FUTURE WORKS

## 5.1 Conclusions

Based on the studies developed in this dissertation it was possible to conclude:

- In Chapter 3, numerical simulations using EbFVM were developed to predict the thermal behavior of autogenous TIG welding process with austenitic stainless steels, using rectangular plates. The simulated thermal cycles were compared with the temperature field of experimental cases from the literature. This comparison showed the good efficiency of the methodology used in these simulations. In a qualitative sense, it was noticed that the compared curves were very close and the temperature fields showed fidelity to the heat transfer phenomenon. The MAPE and CV performance indices gave good quantitative insight into the low errors generated in thermal cycle comparisons. Furthermore, it was possible to analyze the influence of spatial and temporal refinements applied in simulations.
- In Chapter 4, deep learning networks were developed to predict the thermal cycle points generated in an autogenous TIG welding process with austenitic stainless steels, using rectangular plates. The two defined types of network construction offer distinct approaches to predicting the same phenomenon, each with its own advantages. One approach provides a simplified model, while the other offers a broader perspective. The database formed through simulations validated in the previous chapter proved sufficient for applying deep learning models. The methodology adopted for building the model, using mean types, varying the number of hidden layers, and varying hyperparameters, proved to be efficient for training the database and returning low test errors. Therefore, it was possible to predict the thermal cycles of simulated cases and have excellent comparisons in a qualitative sense. Finally, this path proved to be an excellent option for predicting this phenomenon, mainly because it has similar efficiency and a much lower computational cost when compared to traditional numerical simulations.

## 5.2 Future works

This work has been concluded, but it has the potential to explore several fronts, such as:

- Develop an experimental study of the TIG welding process to generate the temperature

field itself and build a deep learning model based on these results;

- A mechanical study of residual stress curves generated in TIG welding process with comparisons between experimental cases, numerical simulations and deep learning predictions;
- The construction of a database with information on thermal cycle curves or residual stresses in different welding processes and materials to have a more generalized and more complete model;
- Develop and compare plastic and viscoplastic models applied to the TIG welding process, using numerical simulation with EbFVM and machine learning.

# REFERENCES


ALPAYDIN, E. **Introduction to Machine Learning**. 2. ed. Cambridge: MIT Press, 2009. (Adaptive Computation and Machine Learning series).

ANGELO, P. C.; BAVISANKAR, B. **Introduction to Steels**: Processing, properties, and applications. Boca Raton: CRC Press, 2019.

ANSARI, M. A.; SAMANTA, A.; BEHNAGH, R. A.; DING, H. An efficient coupled eulerian-lagrangian finite element model for friction stir processing. **The International Journal of Advanced Manufacturing Technology**, [S.l.], v. 101, n. 5-8, p. 1495-1508, 2018.

ASADI, P.; ALIMOHAMMADI, S.; KOHANTORABI, O.; FAZLI, A.; AKBARI, M. Effects of material type, preheating and weld pass number on residual stress of welded steel pipes by multi-pass tig welding (c-mn, sus304, sus316). **Thermal Science and Engineering Progress**, [S.l.], v. 16, p. 100462, 2020.

BERN, M.; PLASSMANN, P. Chapter 6 - mesh generation. *In*: SACK, J.-R.; URRUTIA, J. (Ed.). **Handbook of Computational Geometry**. Amsterdam: North-Holland, 2000. p. 291-332.

BOTTOU, L. Stochastic gradient descent tricks. *In*: ____. **Neural Networks**: Tricks of the trade. 2. ed. Berlin, Heidelberg: Springer Berlin Heidelberg, 2012. p. 421-436.

CAI, W.; WANG, J.; ZHOU, Q.; YANG, Y.; JIANG, P. Equipment and machine learning in welding monitoring: A short review. *In*: THE INTERNATIONAL CONFERENCE ON MECHATRONICS AND ROBOTICS ENGINEERING, 5., 2019, Rome, Italy. Proceedings [...]. New York, NY, USA: Association for Computing Machinery, 2019. p. 9–15.

CARMO, D. A.; FARIA, A. R. A 2d finite element with through the thickness parabolic temperature distribution for heat transfer simulations including welding. **Finite Elements in Analysis and Design**, [S.l.], v. 93, p. 85-95, 2015.

CHAKRAVERTY, S.; MAHATO, N.; KARUNAKAR, P.; RAO, T. **Advanced Numerical and Semi-Analytical Methods for Differential Equations**. Hoboken: Wiley, 2019.

CORDAZZO, J. **Simulação de reservatórios de petróleo utilizando o método EbFVM e multigrid algébrico**. 2006. Phd Thesis (Phd Degree in Mechanical Engineering) — Universidade Federal de Santa Catarina, Florianópolis, 2006.

CORRIGAN, O. **An Investigation Into Machine Learning Solutions Involving Time Series Across Different Problem Domains**. 2018. Phd Thesis (Phd Degree in Computing) — Dublin City University, Dublin, 2018.

DEPRADEUX, L. **Simulation Numerique du Soudage - Acier 316L**: Validation sur cas tests de complexite croissante. 2004. Phd Thesis (Phd Degree in Civil Engineering) — L'insitut National des Sciences Appliquees de Lyon, Lyon, 2004.

DRAMICANIN, M.; BALOS, S.; JANJATOVIC, P.; ZABUNOV, I.; GRABULOV, V. Activated flux TIG welding of stainless steel pipes. **Chemical Industry and Chemical Engineering Quarterly**, [S.l.], v. 25, n. 4, p. 353-360, 2019.

FAVERO, L.; BELFIORE, P. **Data Science for Business and Decision Making**. Cambridge: Elsevier Science, 2019.

FAVI, C.; CAMPI, F.; GERMANI, M.; MANDOLINI, M. A data framework for environmental assessment of metal arc welding processes and welded structures during the design phase. **The International Journal of Advanced Manufacturing Technology**, [S.l.], v. 105, n. 1-4, p. 967-993, 2019.

FILIPPINI, G. **O método de volumes finitos baseado em elementos aplicado a problemas de elasticidade**. 2011. Phd Thesis (Phd Degree in Mechanical Engineering) — Universidade Federal de Santa Catarina, Florianópolis, 2011.

FRENCH, R.; MARIN-REYES, H.; BENAKIS, M. Advanced real-time weld monitoring evaluation demonstrated with comparisons of manual and robotic tig welding used in critical nuclear industry fabrication. *In*: TRZCIELINSKI, S. (Ed.). **Advances in Ergonomics of Manufacturing**: Managing the enterprise of the future. Cham: Springer International Publishing, 2018. p. 3-13.

GARG, H.; SEHGAL, K.; LAMBA, R.; KAJAL, G. A systematic review: Effect of tig and a-tig welding on austenitic stainless steel. *In*: SHANKER, K.; SHANKAR, R.; SINDHWANI, R. (Ed.). **Advances in Industrial and Production Engineering**. Singapore: Springer Singapore, 2019. p. 375-385.

GAUTAM, L.; ANSARI, S.; KHANNA, P. Prediction of angular distortion of angular distortion in gta welded stainless steel 304 plates by mathematical modelling. **International Research Journal of Engineering and Technology (IRJET)**, [S.l.], v. 6, n. 7, p. 1834-1841, 2019.

GLOROT, X.; BENGIO, Y. Understanding the difficulty of training deep feedforward neural networks. *In*: THE INTERNATIONAL CONFERENCE ON ARTIFICIAL INTELLIGENCE AND STATISTICS, 13., 2010, Sardinia, Italy. Proceedings of Machine Learning Research. Chia Laguna Resort, Sardinia, Italy: PMLR, 2010. v. 9, p. 249-256.

GOLDAK, J. A.; AKHLAGHI, M. **Computational Welding Mechanics**. New York: Springer, 2005.

GOODFELLOW, Y. B. I.; COURVILLE, A. **Deep Learning**. Cambridge: The MIT Press, 2016.

GUIMARÃES, J. B. **Estudo dos Parâmetros de Soldagem em um Revestimento de Aço Martensítico 410 NiMo pelo Processo FCAW Pulsado Utilizando Modelos de Regressão**. 2020. Dissertation (Master Degree in Mechanical Engineering) — Universidade Federal do Paraná, Cornélio Procópio, 2020.

GUR, C.; PAN, J. **Handbook of Thermal Process Modeling Steels**. Boca Raton: CRC Press, 2008.

HEATON, J. **Artificial Intelligence for Humans**: Deep learning and neural networks. Chesterfield: Heaton Research, Incorporated., 2015. (Artificial Intelligence for Humans).

HEUMANN, C.; SCHOMAKER, M. **Introduction to Statistics and Data Analysis**: With exercises, solutions and applications in r. Cham: Springer International Publishing, 2017.

HOLMBERG, B. **Stainless steels – their properties and their suitability for welding**. [S.l.]: AvestaPolarit Welding, 2002.

JEONG, W.; SEONG, J. Comparison of effects on technical variances of computational fluid dynamics (cfd) software based on finite element and finite volume methods. **International Journal of Mechanical Sciences**, [S.l.], v. 78, p. 19-26, 2014.

JIAO, W.; WANG, Q.; CHENG, Y.; ZHANG, Y. End-to-end prediction of weld penetration: A deep learning and transfer learning based method. **Journal of Manufacturing Processes**, [S.l.], v. 63, p. 191-197, 2021.

JOO, S.-M.; BANG, H.-S.; BANG, H.-S.; PARK, K.-S. Numerical investigation on welding residual stress and out-of-plane displacement during the heat sink welding process of thin stainless steel sheets. **International Journal of Precision Engineering and Manufacturing**, [S.l.], v. 17, n. 1, p. 65-72, 2016.

KARKHIN, V. **Thermal Processes in Welding**. Singapore: Springer Singapore, 2019. (Engineering Materials).

KESSE, M. A.; BUAH, E.; HANDROOS, H.; AYETOR, G. K. Development of an artificial intelligence powered tig welding algorithm for the prediction of bead geometry for tig welding processes using hybrid deep learning. **Metals**, [S.l.], v. 10, n. 4, 2020.

KUTELU, B. J.; SEIDU, S. O.; EGHABOR, G. I.; IBITOYE, A. I. Review of GTAW welding parameters. **Journal of Minerals and Materials Characterization and Engineering**, [S.l.], v. 06, n. 05, p. 541-554, 2018.

LECUN, Y.; BENGIO, Y.; HINTON, G. Deep learning. **Nature**, [S.l.], v. 521, n. 7553, p. 436–444, 2015.

LINDGREN, L.-E. **Computational welding mechanics**: Thermomechanical and microstructural simulations. Cambridge, England Boca Raton: Woodhead Maney Pub. CRC Press, 2007.

LIPPOLD, J.; KOTECKI, D. **Welding Metallurgy and Weldability of Stainless Steels**. New Jersey: John Wiley & Sons, 2005.

MAHADEVAN, R. R.; JAGAN, A.; PAVITHRAN, L.; SHRIVASTAVA, A.; SELVARAJ, S. K. Intelligent welding by using machine learning techniques. **Materials Today: Proceedings**, [S.l.], v. 46, p. 7402-7410, 2021. Presented in 3rd International Conference on Materials, Manufacturing and Modelling, 2021, [Vellore, India].

MALIK, A. M.; QURESHI, E. M.; DAR, N. U.; KHAN, I. Analysis of circumferentially welded thin-walled cylinders to investigate the effects of varying clamping conditions. **Proceedings of the Institution of Mechanical Engineers, Part B: Journal of Engineering Manufacture**, [S.l.], v. 222, n. 7, p. 901-914, 2008.

MALISKA, C. R. **Heat Transfer and Computational Fluid Mechanics (In Portuguese)**. 2. ed. Rio de Janeiro: LTC, 2004.

MALLICK, P. **Materials, Design and Manufacturing for Lightweight Vehicles**. Cambridge: Woodhead Publishing Limited, 2010. (Woodhead Publishing in Materials).

MARQUES, P.; MODENESI, P.; BRACARENSE, A. **Soldagem - fundamentos e tecnologia**. 3. ed. Belo Horizonte: UFMG, 2011.

MARTíNEZ, R. T.; BESTARD, G. A.; SILVA, A. M. A.; ALFARO, S. C. A. Analysis of gmaw process with deep learning and machine learning techniques. **Journal of Manufacturing Processes**, [S.l.], v. 62, p. 695-703, 2021.

MCGUIRE, M. **Stainless Steels for Design Engineers**. Cleveland: ASM International, 2008. (EngineeringPro collection).

MESSLER, R. **Principles of Welding**: Processes, physics, chemistry, and metallurgy. New York: John Wiley & Sons, 2008.

MIYATA, Y.; OKUGAWA, M.; KOIZUMI, Y.; NAKANO, T. Inverse columnar-equiaxed transition (cet) in 304 and 316l stainless steels melt by electron beam for additive manufacturing (am). **Crystals**, [S.l.], v. 11, n. 8, p. 856, 2021.

MUKHERJEE, T.; MANVATKAR, V.; DE, A.; DEBROY, T. Mitigation of thermal distortion during additive manufacturing. **Scripta Materialia**, [S.l.], v. 127, p. 79-83, 2017.

MÜLLER, A.; GUIDO, S. **Introduction to Machine Learning with Python**: A guide for data scientists. Sebastopol: O'Reilly Media, Incorporated, 2016.

NORRISH, J. **Advanced Welding Processes**. Cambridge: Woodhead Publishing, 2006. (Woodhead Publishing Series in Welding and Other Joining Technologies).

PANDYA, D.; BADGUJAR, A.; GHETIYA, N. A novel perception toward welding of stainless steel by activated tig welding: A review. **Materials and Manufacturing Processes**, Taylor & Francis, [S.l.], v. 36, n. 8, p. 877-903, 2021.

PAVAN, A. R.; ARIVAZHAGAN, B.; ZUBAIRUDDIN, M.; MAHADEVAN, S.; VASUDEVAN, M. Thermomechanical analysis of a-TIG and MP-TIG welding of 2.25cr-1mo steel considering phase transformation. **Journal of Materials Engineering and Performance**, [S.l.], v. 28, n. 8, p. 4903-4917, 2019.

PIMENTA, P. V. C. L.; MARCONDES, F. Two-dimensional rate-independent plasticity using the element-based finite volume method. **Journal of the Brazilian Society of Mechanical Sciences and Engineering**, Springer Science and Business Media LLC, [S.l.], v. 41, n. 3, 2019.

PLAUT, R. L.; HERRERA, C.; ESCRIBA, D. M.; RIOS, P. R.; PADILHAA, A. F. A short review on wrought austenitic stainless steels at high temperatures: Processing, microstructure, properties and performance. **Materials Research**, [S.l.], v. 10, n. 5, p. 453-460, 2007.

RUMELHART, D. E.; HINTON, G. E.; WILLIAMS, R. J. Learning representations by back-propagating errors. **Nature**, [S.l.], v. 323, n. 6088, p. 533-536, Oct. 1986.

SARKAR, S. S.; DAS, A.; PAUL, S.; MALI, K.; GHOSH, A.; SARKAR, R.; KUMAR, A. Machine learning method to predict and analyse transient temperature in submerged arc welding. **Measurement**, [S.l.], v. 170, p. 108713, 2021.

SHAO, C.; CUI, H.; LU, F.; LI, Z. Quantitative relationship between weld defect characteristic and fatigue crack initiation life for high-cycle fatigue property. **International Journal of Fatigue**, [S.l.], v. 123, p. 238-247, 2019.

SHINDE, P. P.; SHAH, S. A review of machine learning and deep learning applications. *In*: INTERNATIONAL CONFERENCE ON COMPUTING COMMUNICATION CONTROL AND AUTOMATION (ICCUBEA), 4., 2018, Pune, India. Proceedings [...]. New Jersey: IEEE, 2019. p. 1-6.

SILVA, R.; DEMARQUE, R.; SANTOS, E. P.; CASTRO, J. A. Influência do aporte térmico sobre as características e propriedades de cordões de solda dos aços aisi 316 e aisi 316l. **Soldagem & Inspeção**, [S.l.], v. 25, 2020.

SINGH, A. K.; DEY, V.; RAI, R. N. Techniques to improveweld penetration in tig welding (a review). **Materials Today - Proceedings**, [S.l.], v. 4, n. 2, Part A, p. 1252-1259, 2017.

SRIVASTAVA, N.; HINTON, G.; KRIZHEVSKY, A.; SUTSKEVER, I.; SALAKHUTDINOV, R. Dropout: A simple way to prevent neural networks from overfitting. **Journal of Machine Learning Research**, [S.l.], v. 15, n. 56, p. 1929-1958, 2014.

STEELS, A. **Atlas Steels Technical Handbook of Stainless Steels**. Newcastle: Atlas Steels Technical Department, 2021.

TIMINGS, R. **Fabrication and Welding Engineering**. Oxford: Newnes, 2008.

VARGHESE, V. M. J.; SURESH, M. R.; KUMAR, D. S. Recent developments in modeling of heat transfer during TIG welding - a review. **The International Journal of Advanced Manufacturing Technology**, [S.l.], v. 64, n. 5-8, p. 749-754, 2012.

VENKATKUMAR, D.; RAVINDRAN, D. 3d finite element simulation of temperature distribution, residual stress and distortion on 304 stainless steel plates using gta welding. **Journal of Mechanical Science and Technology**, [S.l.], v. 30, n. 1, p. 67-76, 2016.

WEMAN, K. 6 - tig welding. *In*: WEMAN, K. (Ed.). **Welding Processes Handbook**. 2. ed. [S.l.]: Woodhead Publishing, 2012, (Woodhead Publishing Series in Welding and Other Joining Technologies). p. 63-69.

XIA, J.; JIN, H. Numerical modeling of coupling thermal–metallurgical transformation phenomena of structural steel in the welding process. **Advances in Engineering Software**, [S.l.], v. 115, p. 66-74, 2018.

XU, Y.; LIMA, I.; MARCONDES, F.; SEPEHRNOORI, K. Development of an embedded discrete fracture model for 2d and 3d unstructured grids using an element-based finite volume method. **Journal of Petroleum Science and Engineering**, [S.l.], v. 195, p. 107725, 2020.

YOUSSEF, H. **Machining of Stainless Steels and Super Alloys**: Traditional and nontraditional techniques. Chichester: John Wiley & Sons, 2016.